

# Quasi-symmetry protected topology in a semi-metal

Chunyu Guo,<sup>1\*</sup> Lunhui Hu,<sup>2\*</sup> Carsten Putzke,<sup>1,3</sup> Jonas Diaz,<sup>1</sup> Xiangwei Huang,<sup>1</sup> Kaustuv Manna,<sup>4,5</sup> Feng-Ren Fan,<sup>4</sup> Chandra Shekhar,<sup>4</sup> Yan Sun,<sup>4</sup> Claudia Felser,<sup>4</sup> Chaoxing Liu,<sup>2,6†</sup> B. Andrei Bernevig,<sup>6,7,8†</sup> Philip J. W. Moll<sup>1†</sup>

<sup>1</sup>Laboratory of Quantum Materials (QMAT), Institute of Materials (IMX),

École Polytechnique Fédérale de Lausanne (EPFL), CH-1015 Lausanne, Switzerland

<sup>2</sup>Department of Physics, The Pennsylvania State University, University Park, PA, USA

<sup>3</sup>Max Planck Institute for the Structure and Dynamics of Matter, 22761 Hamburg, Germany

<sup>4</sup>Max Planck Institute for Chemical Physics of Solids, 01187 Dresden, Germany

<sup>5</sup>Department of Physics, Indian Institute of Technology Delhi, New Delhi 110016, India

<sup>6</sup>Department of Physics, Princeton University, Princeton, New Jersey 08544, USA

<sup>7</sup>Donostia International Physics Center, P. Manuel de Lardizabal 4, 20018

Donostia-San Sebastian, Spain

<sup>8</sup>IKERBASQUE, Basque Foundation for Science, Bilbao, Spain

\*These authors contributed equally to this work.

†Corresponding authors: cxl56@psu.edu(C.X.L.); bernevig@princeton.edu(B.A.B.); philip.moll@epfl.ch(P.J.W.M.)

**The crystal symmetry of a material dictates the type of topological band structures it may host, and therefore symmetry is the guiding principle to find topological materials. Here we introduce an alternative guiding principle, which we call ‘quasi-symmetry’. This is the situation where a Hamiltonian has an exact symmetry at lower-order that is broken by higher-order perturbation terms. This enforces finite but parametrically small gaps at some low-symmetry points in momentum space. Untethered from the restraints of symmetry, quasi-symmetries eliminate the need for fine-tuning as they enforce**

**that sources of large Berry curvature will occur at arbitrary chemical potentials. We demonstrate that a quasi-symmetry in the semi-metal CoSi stabilizes gaps below 2 meV over a large near-degenerate plane that can be measured in the quantum oscillation spectrum. The application of in-plane strain breaks the crystal symmetry and gaps the degenerate point, observable by new magnetic breakdown orbits. The quasi-symmetry, however, does not depend on spatial symmetries and hence transmission remains fully coherent. These results demonstrate a class of topological materials with increased resilience to perturbations such as strain-induced crystalline symmetry breaking, which may lead to robust topological applications as well as unexpected topology beyond the usual space group classifications.**

The introduction of concepts of topology in the past years into the field of electronic dispersions has captured the imagination of condensed matter physics and sparked a flurry of new research directions. In topologically non-trivial metals, the wavefunctions are inherently non-local, and novel electronic states are expected and observed at the crystal surface terminating them (1–10). Beyond these surface properties, interesting anomalies in the bulk dispersion lead to novel physical phenomena, such as the emergence of quasiparticles mimicking ultra-relativistic Weyl- and Dirac-Fermions in 3D; a solid-state analogon of the Adler-Bell-Jackiw anomaly; a planar Hall effect; topological piezoelectric effect; second harmonic generation in Weyl semimetals; or strong Berry curvature that impacts the semi-classical and quantum dynamics of quasiparticles (11–19).

Given the wealth of new phenomena and potential applications, it is important to identify such "ideal" Weyl-, Dirac- or nodal-line semi-metals in which the a priori unrelated chemical potential and the topological anomaly coincide. That such a coincidence is rather rare can be understood from the Wigner-Von Neumann theorem, which states that a two-level crossing

generally requires three tuning parameters (20, 21). To stabilize crossings of more than two bands (nodal points) or achieve higher dimensional degeneracies (nodal lines, planes), additional crystalline symmetries must provide further constraints on the form of the Hamiltonian, such as rotational symmetries for the fourfold Dirac points in the 3D Dirac semi-metals  $\text{Cd}_3\text{As}_2$  and  $\text{Na}_3\text{Bi}$  (6, 7) or two-fold screw axis for the nodal plane in  $\text{MnSi}$  (22).

Hence crystalline symmetry and band topology are inseparably intertwined, and it is natural that symmetry should guide our search for materials. Here we refine this picture, and argue for the importance of approximate symmetries as an additional concept (Fig. 1) with clearly observable experimental consequences. A crystalline symmetry operation,  $M$ , commutes with the Hamiltonian of the system,  $[H(k), M] = 0$ . The well-known representation theory dictates that low-symmetry points usually support only one-dimensional representations, and hence bands anti-cross at these points. It may be possible, however, that at these low symmetry points *approximate* symmetries emerge. They are not exact symmetries of the crystal yet still commute with a dominant part of the Hamiltonian. Such approximate symmetries would stabilize almost linear band crossings by enforcing finite yet perturbatively small energy gaps. A trivial example is a weak lattice distortion that removes a spatial symmetry that otherwise stabilizes a band crossing. Graphene could be considered as an alternative example in the spin channel, as its Dirac point is weakly gapped when spin-orbit coupling is considered, turning spin-rotation into an approximate symmetry (23, 24). However, as approximate symmetries leave the bounds set by crystalline point-groups, more exciting approximate symmetries may emerge that have no counterpart in the crystal symmetry.

We adopt the term “quasi-symmetry” to denote a special type of approximate symmetry of electronic band structures, that emerges from the hierarchy of a  $k \cdot p$  type of perturbation expansion around a high-symmetry point. Quasi-symmetries are operators  $M_{eff}$  that are the *exact* symmetries of the lower-order expansion but not of higher-order perturbation terms. The

main goal of this paper is to show such a quasi-symmetry exists in the semi-metal CoSi as well as a large set of similar materials, and that it enforces a low-symmetry plane of near-degeneracies spanning the Brillouin zone which pin a source of Berry curvature to the Fermi level (Fig. 2). Excitingly, it falls into the latter category of quasi-symmetries that are unrelated to approximate point-group symmetries, but can be treated as a symmetry of internal degrees of freedom, akin to spin in graphene. Unlike graphene, however, the form of quasi-symmetry is non-trivial as the corresponding symmetry operator is generally  $k$ -dependent and forms a part of the Hamiltonian. The key distinction is that while a proper crystal symmetry acts on all atomic coordinates uniformly, the quasi-symmetry operation exchanges 3d orbitals on subsets of inequivalent Co-sites selectively. A simplified example may be an incomplete mirror image [Fig. 1(a) and (b)], in which the mirror operation acts only on parts of the object but not the whole consistently.

CoSi crystallizes in a chiral cubic structure of space group  $P2_13$  without an inversion center (Fig. 2). Recent studies revealed the existence of exceptionally long Fermi arcs which connect the sixfold and fourfold band degenerate points (9, 25–27). These two degenerate points correspond to two branches of Fermi surfaces located at the  $\Gamma$ - and R-point, respectively, yet only the R-point pockets are observed in quantum oscillation experiments. Band structure calculations reveal four split bands due to spin-orbit coupling which correspond to four Fermi surfaces at R, which we label as  $1^+$ ,  $1^-$ ,  $2^+$ ,  $2^-$ , representing the orbital and spin degree of freedom respectively. States at the boundary of the Brillouin zone are doubly degenerate due to crystalline symmetry, hence the non-degenerate Fermi surfaces are enforced to touch there (5). The spin-orbit coupling and the orbital gap are both small yet similar in magnitude, which explains how four slightly degenerate, interpenetrating spheroids make up a surprisingly rich internal structure of the Fermi surfaces.

CoSi single crystals resemble octahedra, indicating a dominant growth along the [111] di-

rection (see supplement Sec.I.A. for growth details). These crystals were fabricated into microstructures using focused-ion-beam machining (28) (see supplement Sec.I.B.) to increase the current path homogeneity and signal of Shubnikov-de Haas oscillations. This microfabrication will later be the key to study the effects of unidirectional strain. The resistivity as well as the large residual resistivity ratio in the samples agrees well with previous bulk measurements (29), indicating an unchanged material quality during fabrication (see supplement Fig. S1). Hence not surprisingly, large quantum oscillations of the magnetoresistance are readily observed at low fields (Fig. 3). Subtracting a polynomial background uncovers strong oscillations that resemble a beating pattern of two frequencies around  $F_1 \sim 550$  T and  $F_2 \sim 660$  T, in good agreement with existing literature (29–32). The temperature dependence of the oscillations follows well the Lifshitz-Kosevich form, leading to a cyclotron effective mass of  $m_c \sim 0.84 m_e$  (see supplement Fig. S14).

In light of the complexity of self-intersecting Fermi surfaces it appears at first surprising that the quantum oscillation spectrum is tantalizingly simple, with only two frequencies that, most importantly, only weakly depend on the direction of the applied magnetic field (Fig. 3). When magnetic quantum oscillations arise from such highly degenerate Fermi surfaces, the main question is which, if any, possible trajectories become quantum coherent. As the Fermi-surface is centered around the R-point, any orbit necessarily crosses the symmetry-enforced degeneracies at the Brillouin zone boundary multiple times. This has been argued to stabilize band degeneracies pinned to the Fermi level in this crystal structure (22, 32) on the planes of Brillouin zone boundary [marked purple in Fig. 4(f)].

Yet the orbits further intersect at low-symmetry points at which a gap must open [marked blue in Fig. 4(f)]. Neither the frequencies nor their angle dependence obtained from DFT calculations match the data if this gap is considered to separate the orbits via significant avoided-crossing. As the gap is small, the quasiparticle can tunnel across it continuing on the original

trajectory, a phenomenon known as magnetic breakdown (33–36). Based on estimations of the gap from DFT and further analytical calculations, vanishingly small breakdown fields fall below 0.11 T for any field orientation, and hence the experimental data is always obtained in an extreme breakdown regime (see supplement Sec. V. for details). Thus the wavefunctions propagate through these points at near-perfect transmission, and indeed an excellent match of frequencies and their angle dispersion between theory and experiment is found (Fig. 3).

These observations raise a key question about the electronic structure, namely why in a metal with eV bandwidth two bands anti-cross with a gap no larger than 2 meV in extended regions of the Brillouin zone. To obtain such a parametrically small gap accidentally, an unreasonable degree of fine-tuning is required that acts simultaneously at many k-points, as well as at a wide range of energies as we will show. Instead, a quasi-symmetry enforces the uniform smallness of this gap, and thus explains why magnetic breakdown at full transparency occurs at any arbitrary angle.

To understand this quasi-symmetry, we next consider an effective model around the R-point. Without spin-orbit coupling (SOC), all the bands are eight-fold degenerate at R due to the combination of two-fold screw axis symmetries along the x and y direction and time reversal symmetry. Including spin doubles the degeneracy and the SOC splits the eight-fold degenerate states into six-fold and two-fold degenerate states at the R-point. An effective model for these eight bands around the R-point can be constructed as

$$\mathcal{H}_R = \mathcal{H}_0(\mathbf{k}) + \mathcal{H}_{soc} + \mathcal{H}_{k^2}(\mathbf{k}), \quad (1)$$

where  $\mathcal{H}_0(\mathbf{k}) = C_0 + 2A_1(\mathbf{k} \cdot \mathbf{L})$  is the lower-order expansion of the spin-independent Hamiltonian, and three 4-by-4 matrices  $\mathbf{L}$  form an emergent angular momentum algebra  $[L_i, L_j] = i\varepsilon_{ijk}L_k$  with Levi-Civita symbol  $\varepsilon_{ijk}$  and  $i, j, k = x, y, z$ . The SOC term is given by  $\mathcal{H}_{soc} = 2\lambda_0(\mathbf{s} \cdot \mathbf{L})$ , where  $\mathbf{s}$  is the spin operator.  $\mathcal{H}_{k^2}(\mathbf{k})$  is the higher-order spin-independent term with

its form given in the supplement. Here  $\mathcal{H}_0(k) + \mathcal{H}_{k^2}(k)$  is the SOC-free expanded Hamiltonian to second order. By choosing appropriate parameters such as  $C_0, A_1, \lambda_0$ , the energy dispersion of  $\mathcal{H}_R$  well reproduces that from the DFT calculations (see supplement Sec. VII.).

A striking feature in the Hamiltonian  $\mathcal{H}_R$  is that the SOC term  $\mathcal{H}_{soc}$  takes a similar form as the linear-momentum term, just by replacing the momentum  $\mathbf{k}$  by spin  $s$ . This is because spin, as a pseudo-vector, behaves exactly the same as a vector due to the lack of inversion, mirror or other roto-inversion symmetries for a chiral crystal. Due to this similarity, up to the first-order perturbation, we find that the spin of the eigen-states is parallel or anti-parallel to the momentum  $\mathbf{k}$  and thus we can label the spin states of these bands by  $\pm$  in Fig. 2(b). We derive an effective Hamiltonian for the near degenerate bands. This can be done by first projecting the full Hamiltonian  $\mathcal{H}_R$  into the 4 closest bands ( $1^\pm$  and  $2^\pm$  bands) to get a 4-band model and then constructing a 2-band model for the  $1^-$  and  $2^+$  bands, as discussed in supplement. Up to the first-order perturbation, the 2-band Hamiltonian takes the form  $H_{eff} = \epsilon_0 + d_z(\mathbf{k})\sigma_z$ , where  $d_z(\mathbf{k}) = \lambda_0 - \sqrt{3}\tilde{C}\frac{|k_x k_y k_z|}{k}$  and the form of the function  $\epsilon_0$  is given in supplement. Here  $\sigma_z$  is the Pauli matrix on the basis of  $1^-$  and  $2^+$  bands,  $\lambda_0$  term comes from the SOC Hamiltonian  $\mathcal{H}_{soc}$  and the  $\tilde{C}$  term from  $\mathcal{H}_{k^2}(\mathbf{k})$ . It is striking to see that the operator  $\mathcal{M}_{eff} = \sigma_z$  commutes with  $H_{eff}$  and thus serves as an *exact* symmetry at the first-order expansion. The existence of  $\mathcal{M}_{eff}$  forbids any terms that are coupled to  $\sigma_{x,y}$  in the effective Hamiltonian, thus reducing the codimension of a two-level crossing from 3 to 1 and stabilizing a nodal plane, which is defined by the equation  $\lambda_0 = \sqrt{3}\tilde{C}\frac{|k_x k_y k_z|}{k}$  in this two-band model. A more accurate and complete description around the Fermi energy is the 4-band model, which shares a similar k-dependent hidden quasi-symmetry and is essential in deriving the 2-band model (see supplement Sec. VII.), and the whole perturbation theory reveals a striking hierarchy structure. Higher-order perturbation expansion breaks  $\mathcal{M}_{eff}$  through inducing additional terms coupled to  $\sigma_{x,y}$  in the effective model and thus leads to a small gap opening of this nodal plane (see supplement).

Therefore,  $\mathcal{M}_{eff}$  is not a symmetry of the system, but an emergent quasi-symmetry in the sense of low-energy effective theory. Importantly, this curved nodal plane spans low-symmetry regions of the Brillouin zone, in contrast to symmetry-enforced exact degeneracies. It is this combined structure of symmetry and quasi-symmetry induced degeneracies that forms the basis of the complex structure of the Fermi surface centered at R, and reduces the complexity of the quantum orbits in magnetic fields to two, angle-independent frequencies.

Physically, quasi-symmetry is linked to the orbital structure of the wavefunctions, and its operation only interchanges the orbitals at different atomic sites (internal degrees). Thus, unlike crystalline symmetries, they remain robust against symmetry-breaking lattice distortions (Fig. 4). This is probed experimentally by the application of tensile strain to a bar cut approximately along the [110] direction. The low-symmetry distortion removes the critical screw symmetries at the zone boundaries, and gaps the otherwise symmetry protected crossing points. Experimentally, such strain can be easily applied by thinning the transport bar by FIB-milling, thus reducing its effective spring constant and increasing the total distortion under equal force. The microstructures are coupled to a sapphire substrate and their differential thermal contraction generates the desired tensile strain along the bar [see supplement and (37)]. As such strain lifts the screw symmetry protecting the degeneracy, one naturally expects the sample to gradually leave the magnetic breakdown regime as the strain is increased and a zoo of sum frequencies to emerge that correspond to all possible area differences between the orbits (34–36). Indeed, the strained bar exhibits pronounced satellite peaks that are symmetrically offset from the main peaks by  $\Delta F \approx 32 T$  for all harmonics. This matches exactly with the calculated area difference between the crystalline symmetry protected points, fully explaining the observed spectrum. However, those areas associated with a quasiparticle tunneling at a quasi-symmetry-protected point are not observed, implying that the magnetic breakdown field associated with that gap remains much smaller than the lowest field at which quantum oscillations are observed.



This is a direct experimental proof that the quasi-symmetry protection is insensitive to breaking of crystalline symmetries, a notion that can be well corroborated by calculations (Fig. 4). This resilience clearly distinguishes symmetry and quasi-symmetry enforced topological band anomalies.

Their unique implications in the Berry curvature distribution in momentum space are another key characteristic of the topological character of near-degeneracies enforced by quasi-symmetry, compared to the exact degeneracies due to symmetry [Fig. 2(f)]. The Berry curvature almost vanishes in the vicinity of the exact degenerate plane, yet it is concentrated to a ring on the near nodal plane at any fixed energy. This large Berry curvature around the near nodal lines, which always occurs at the Fermi energy, may strongly affect physical phenomena that are related to local Berry curvature, including intrinsic spin Hall effect (38, 39) and quantum non-linear Hall effect (40).

The quasi-symmetry is the mathematical and physical framework behind the unexpectedly simple and strain-resistant quantum oscillation spectrum of CoSi. It is, however, just one example of a large class of materials in which quasi-symmetries can exist. Clearly, this new class of near degenerate manifolds at low-symmetry  $k$ -points is not found by current search programs for topological materials based on crystalline symmetry without further guideline. To search for materials with quasi-symmetries, a systematic expansion of the  $k \cdot p$ -type effective Hamiltonian order by order is required for all space groups, which is in principle feasible (41). Typically, lower-order terms with higher symmetries than the crystalline symmetry itself possess larger prefactors than the higher-order terms with lower symmetries (42), and a symmetry hierarchy is expected for the terms of different orders in the  $k \cdot p$ -type Hamiltonian. Further interesting flavors of quasi-symmetry may exist which emerge when higher-order terms with additional symmetries become dominant. Experimentally, we propose that quantum oscillations may provide guidance by pointing to materials with similarly extreme magnetic breakdown on extended

regions on the Fermi surface, which a quasi-symmetry would naturally explain. While the here described search methods need to be implemented in the future, it is natural to anticipate quasi-symmetries in related compounds crystallizing in the same structure, such as e.g. PtGa, PtAl, RhSi and the magnetic MnSi where the influence of magnetism can be explored. (22, 43–51). Our DFT calculations indeed reveal similar energy dispersions and Fermi surface shapes with quasi-symmetry-induced near degeneracies in PtAl, PtGa and RhSi (see supplement Sec. VI.). The concept of the quasi-symmetry raises the interesting prospect that even those materials in which crystalline symmetries do not allow stable band crossings may still host exotic quasi-particles and strong Berry curvature at the Fermi level. If such features at the Fermi level are desired, the current approach of automated symmetry classifications may not prove to lead to the most practical materials. Without the necessity of a crystalline symmetry protecting higher-order band crossing points, quasi-symmetries hold an advantage for topological applications. The topological anomalies in real materials often are far away from the Fermi level, and in thin-film form they are exposed to mismatch strains inherent to heterostructures. These key bottlenecks of topological materials do not restrict quasi-symmetric materials. A consensus of high-throughput efforts emerges that 20-30% of materials are topological (52–55). Yet it appears that crystal symmetry may not hold up as the strict barrier it was thought to be, and via quasi-symmetries concepts, topology may reach even further than these estimates predict.

**Acknowledgements** We would like to acknowledge Dr. Joerg Harms for the assistance on graphic design. This work was funded by the European Research Council (ERC) under the European Union’s Horizon 2020 research and innovation programme (MiTopMat - grant agreement No. 715730). This project received funding by the Swiss National Science Foundation (Grants No. PP00P2\_176789). C. X. Liu and L. H. Hu are supported by the Office of Naval Research (Grant No. N00014-18-1-2793) and Kaufman New Initiative research Grant No. KA2018-98553 of the Pittsburgh Foundation. K.M., and C.F. acknowledge the financial support from the European Research Council (ERC) Advanced Grant No. 742068 ”TOP-MAT”; European Union’s Horizon 2020 research and innovation program (Grant Nos. 824123 and 766566)and Deutsche Forschungsgemeinschaft (DFG) through SFB 1143. Additionally, K. M. acknowledges Max Plank Society for the funding support under Max Plank–India partner group project. B.A.B. thanks funding from the European Research Council (ERC) under the European Union’s Horizon 2020 research and innovation programme (grant agreement no. 101020833). B.A.B. is also supported by the U.S. Department of Energy (Grant No. DE-SC0016239), and partially supported by the National Science Foundation (EAGER Grant No. DMR 1643312), a Simons Investigator grant (No. 404513), the Office of Naval Research (ONR Grant No. N00014-20-1-2303), the Packard Foundation, the Schmidt Fund for Innovative Research, the BSF Israel US foundation (Grant No. 2018226), the Gordon and Betty Moore Foundation through Grant No. GBMF8685 towards the Princeton theory program, and a Guggenheim Fellowship from the John Simon Guggenheim Memorial Foundation. B.A.B. and C. X. Liu is supported by the NSF-MERSEC (Grant No. MERSEC DMR 2011750). B.A.B. gratefully acknowledge financial support from the Schmidt DataX Fund at Princeton University made possible through a major gift from the Schmidt Futures Foundation. B.A.B. received additional support from the Max Planck Society. Further support was provided by the NSF-MRSEC No. DMR-1420541, BSF Israel US foundation No. 2018226, and the Princeton Global Network

Funds.

**Author Contributions** C.C. and L.H. contributes equally to this work. Crystals were synthesized and characterized by K.M., C.S. and C.F.. The experiment design, FIB microstructuring and the magnetotransport measurements were performed by C.G., C.P., J.D., X.H. and P.J.W.M.. L.H., C.L. and B.A.B. developed and applied the general theoretical framework, and the analysis of experimental results has been done by C.G. C.P. and P.J.W.M.. Band structures were calculated by Y.S. F.F. and C.F.. All authors were involved in writing the paper.

**Competing Interests** The authors declare that they have no competing financial interests.

## **Methods**

### **Data Availability**

Data that support the findings of this study is deposited to Zendo with the access link: <https://doi.org/10.5281/zenodo.6336000>.

### **Code Availability**

Matlab code used for this study is deposited to Zendo with the access link: <https://doi.org/10.5281/zenodo.6336013>.

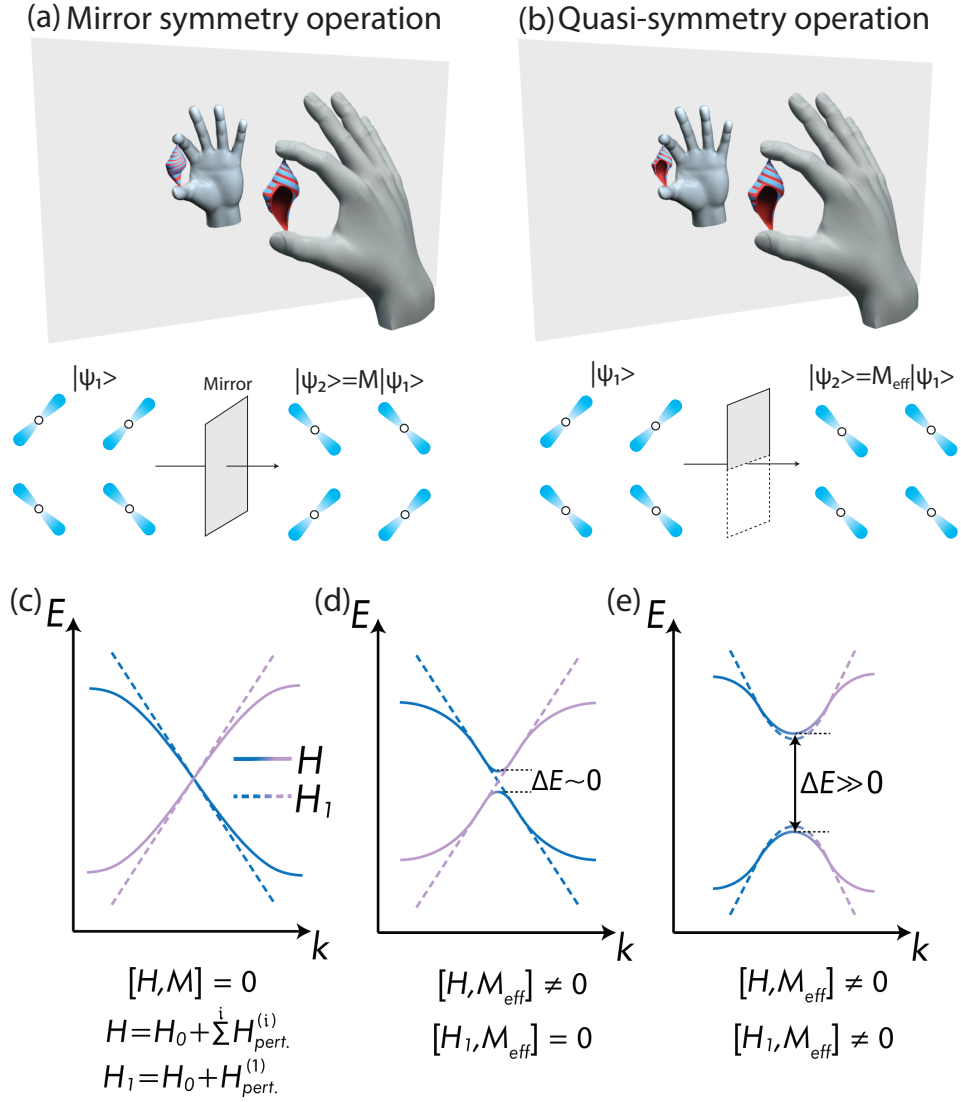


Figure 1: (a) Illustration of a mirror symmetry operation, which acts at the whole object consistently. (b) In contrast to the mirror symmetry, quasi-symmetry operation acts differently on different parts of the system. (c) If a crystalline symmetry operation commutes with the Hamiltonian system, the band crossing point is therefore symmetry-protected. (d) In this case the Hamiltonian itself does not commute with the symmetry operation yet its first order perturbation does. This lead to the situation where though the band crossing is numerically avoided but the resulted gap size is negligible for the physical properties of the system. This type of symmetry is called quasi-symmetry. (e) If the symmetry operation does not commute with the Hamiltonian to any order of perturbation of the system, the crossing is not protected by any symmetry. This will result in a sizeable gap and lost of topological character.

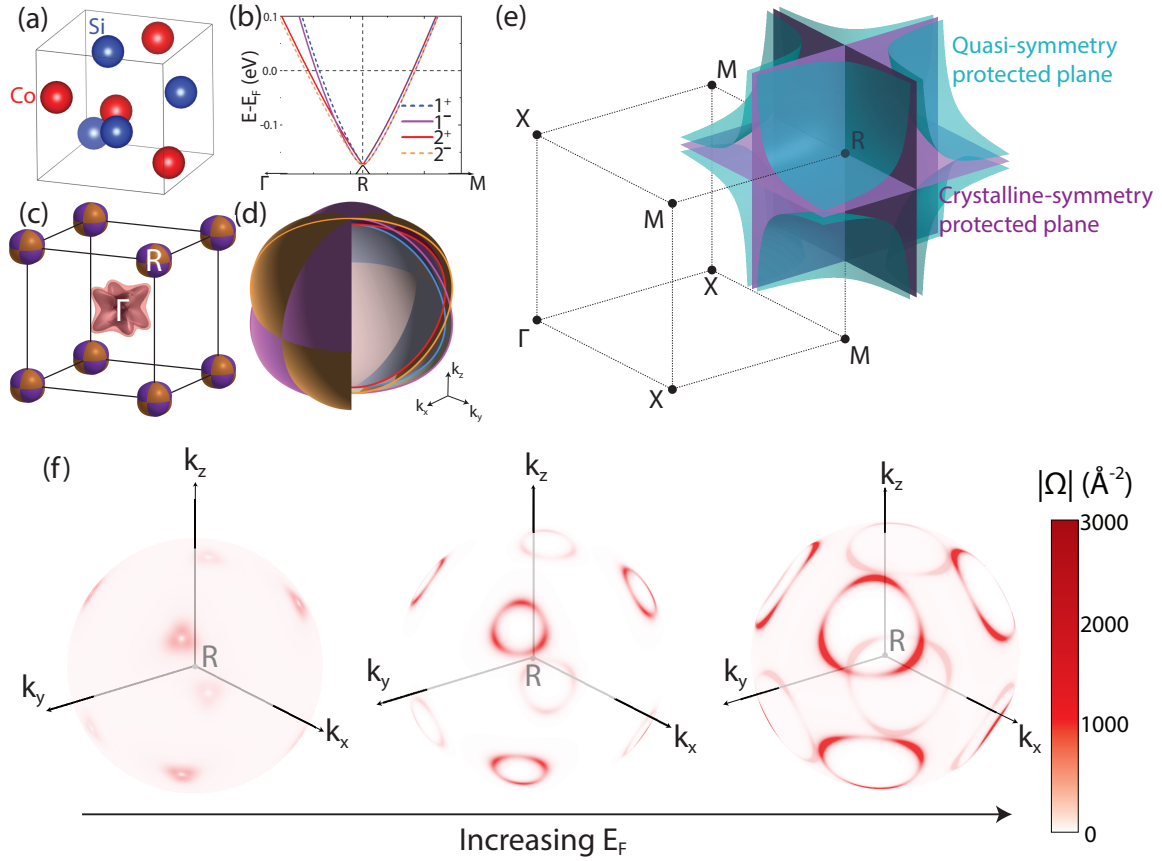


Figure 2: (a) Crystal structure of CoSi. Co and Si atoms are presented as red and blue spheres respectively. (b) Ab-initio-calculated band structure of CoSi around R-point. Here  $1/2$  denotes orbital character while  $+/-$  stands for the spin character of the band. (c) 3D view of all Fermi surfaces, which are centered around either R- or  $\Gamma$ - point of the Brillouin zone. (d) 3D view of Fermi surfaces centered around R-point with a quadrant cut. (e) Quasi-symmetry and crystalline-symmetry protected degenerate planes. (f) The Berry curvature distribution of the  $1^-$ -band defined in (b) at different Fermi energy calculated from the model Hamiltonian Eq. (1).

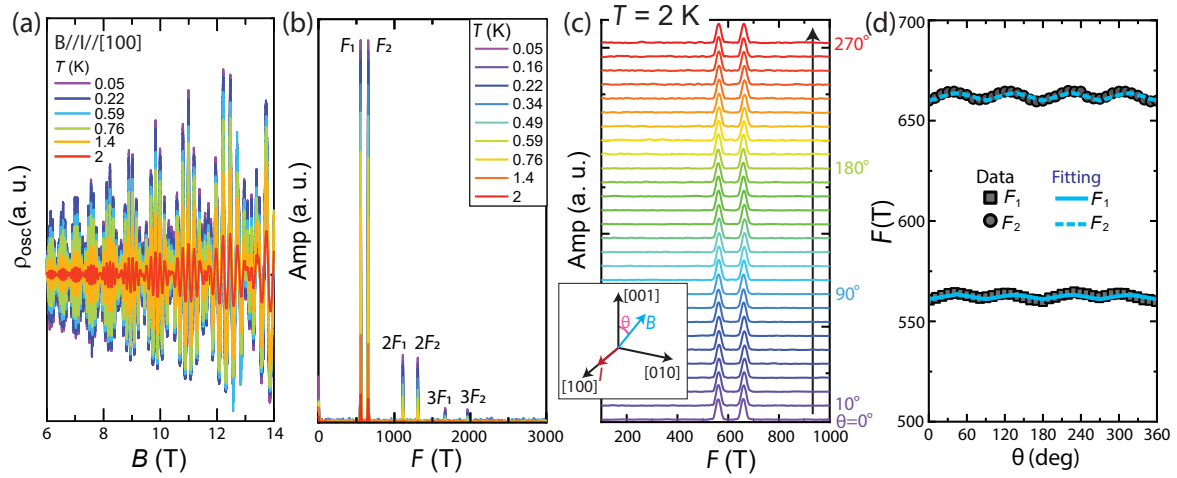


Figure 3: (a) Temperature-dependent SdH oscillations with field and current applied along [100] axis. Here  $\rho_{osc} = \Delta\rho/\rho_{BG}$ , with  $\Delta\rho$  the oscillatory part of the magnetoresistivity, and  $\rho_{BG}$  the background obtained from a 3<sup>rd</sup>-order polynomial fit to the magnetoresistivity. (b) Fast-Fourier-transformation spectrum of the SdH oscillations presented in (a) with the field window of 3 to 14 T. Two main peaks, as well as their higher-harmonic components, can be clearly observed. The suppression of peak amplitude with increasing temperature is due to the thermal damping effect. (c) Fast-fourier-transformation (FFT) spectrum of angle-dependent quantum oscillations measured at  $T = 2$  K. Here the magnetic field is rotated within (100) plane and the angle is defined between the field direction and [001] axis. (d) Summary of angular dependence of oscillation frequencies. Here the fitting is generated by calculating the orbital area based on band structure calculations with taking extrem magnetic breakdown due to quasi-symmetry into account (see supplement). The near-perfect fitting clearly demonstrates that quasi-symmetry is the only option to explain the experimental results of nearly angle-independent oscillation frequencies.

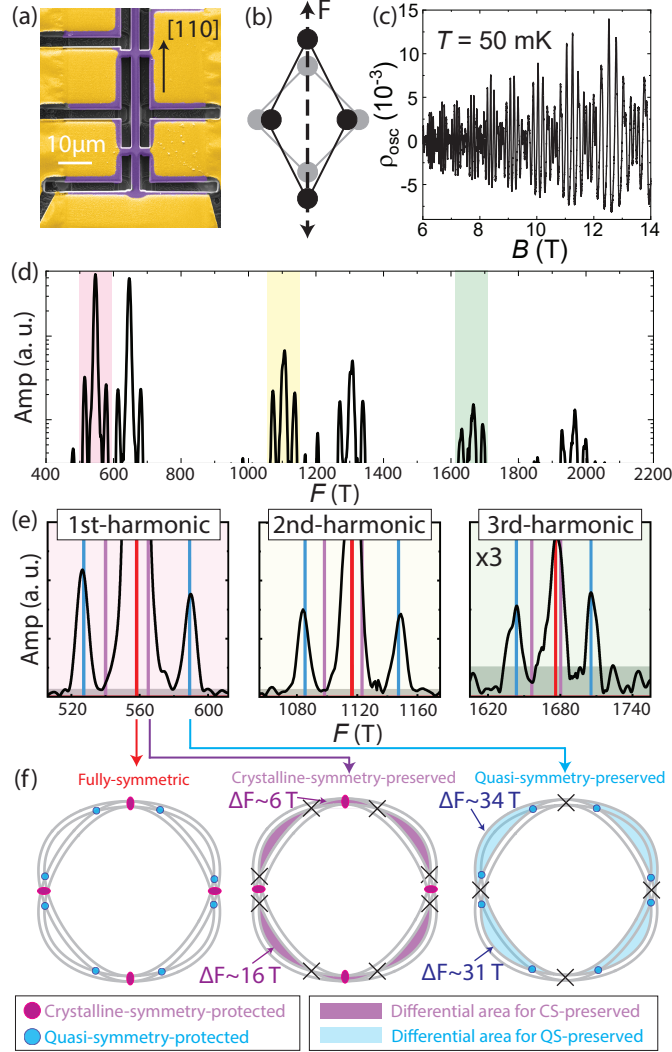


Figure 4: (a) Scanning electron microscope image of CoSi microdevice. A long bar roughly along  $[110]$  direction with a  $2.5$  by  $2.4 \mu\text{m}^2$  cross section is fabricated by FIB. (b) Illustration of tensile strain approximately along  $[110]$  which breaks the  $C_2$  rotational symmetry of the crystal structure. (c) SdH oscillations with both field and current applied along the fabricated bar direction at  $T = 50$  mK. (d) Logarithmic-scaled FFT spectrum of SdH oscillations displayed in (c). The main peaks are always accompanied with satellite peaks up to the third harmonics. (e) Enlarged view of satellite peaks correspond to the  $1^{\text{st}}$  to  $3^{\text{rd}}$  harmonic oscillations. The red, purple and blue vertical lines correspond to the FFT spectrum produced by the fully symmetric, crystalline-symmetry-preserved and quasi-symmetry-preserved scenarios respectively. (f) Corresponding Landau orbits for three different scenarios. Here the colored area illustrates the orbital area difference compared to the fully-symmetric case, and the black crosses represent the degeneracies that are lifted in different scenarios. Only the quasi-symmetry-preserved scenario reproduces FFT peaks that match perfectly well with the experimental data.



## References

1. Armitage, N. P., Mele, E. J., and Vishwanath, A. Weyl and Dirac semimetals in three-dimensional solids. *Rev. Mod. Phys.* **90**, 015001 (2018).
2. Lv, B. Q., Qian, T., and Ding, H. Experimental perspective on three-dimensional topological semimetals. *Rev. Mod. Phys.* **93**, 025002 (2021).
3. Wan, X. G., Turner, A. M., Vishwanath, A., and Savrasov, S. Y. Topological semimetal and Fermi-arc surface states in the electronic structure of pyrochlore iridates. *Phys. Rev. B* **83**, 205101 (2011).
4. Wang, Z., Alexandradinata, A., Cava, R. J., and Bernevig, B. A. Hourglass fermions. *Nature* **532**, 189–194 (2016).
5. Bradlyn, B., Cano, J., Wang, Z., Vergniory, M. G., Felser, C., Cava, R. J., and Bernevig, B. A. Beyond Dirac and Weyl fermions: Unconventional quasiparticles in conventional crystals. *Science* **353**, aaf5037 (2016).
6. Wang, Z., Sun, Y., Chen, X.-Q., Franchini, C., Xu, G., Weng, H., Dai, X., and Fang, Z. Dirac semimetal and topological phase transitions in  $A_3Bi$  ( $A=Na, K, Rb$ ). *Phys. Rev. B* **85**, 195320 (2012).
7. Wang, Z., Weng, H., Wu, Q., Dai, X., and Fang, Z. Three-dimensional Dirac semimetal and quantum transport in  $Cd_3As_2$ . *Phys. Rev. B* **88**, 125427 (2013).
8. Bian, G., Chang, T., Zheng, H., Velury, S., Xu, S.-Y., and Neupert, T. et al., Drumhead surface states and topological nodal-line fermions in  $TlTaSe_2$ . *Phys. Rev. B* **93**, 121113 (2016).

9. Rao, Z., Li, H., Zhang, T., Tian, S., Li, C., and Fu, B. et al., Observation of unconventional chiral fermions with long Fermi arcs in CoSi. *Nature* **567**, 496–499 (2019).
10. Moll, P. J. W., Nair, N. L., Helm, T., Potter, A. C., Kimchi, I., Vishwanath, A., and Analytis, J. G. Transport evidence for Fermi-arc-mediated chirality transfer in the Dirac semimetal  $\text{Cd}_3\text{As}_2$ . *Nature* **535**, 266–270 (2016).
11. Zyuzin, A. A., and Burkov, A. A. Topological response in Weyl semimetals and the chiral anomaly. *Phys. Rev. B* **86**, 115133 (2012).
12. Burkov, A. A. Chiral anomaly and transport in Weyl metals. *J. Condens. Matter Phys.* **27**, 113201 (2015).
13. Xiong, J., Kushwaha, S. K., Liang, T., Krizan, J. W., Hirschberger, M., and Wang, W. et al., Evidence for the chiral anomaly in the Dirac semimetal  $\text{Na}_3\text{Bi}$ . *Science* **350**, 413-416 (2015).
14. Matsushita, T., Fujimoto, S., and Schnyder, A. P. Topological piezoelectric effect and parity anomaly in nodal line semimetals. *Phys. Rev. Research* **2**, 043311 (2020).
15. Li, Z., Jin, Y.-Q., Tohyama, T., Iitaka, T., Zhang, J.-X., and Su, H. Second harmonic generation in the Weyl semimetal TaAs from a quantum kinetic equation. *Phys. Rev. B* **97**, 085201 (2018).
16. Takasan, K., Morimoto, T., Orenstein, J., and Moore, J. E. Current-induced second harmonic generation in inversion-symmetric Dirac and Weyl semimetals. *Phys. Rev. B* **104**, L161202 (2021).
17. Burkov, A. A. Giant planar Hall effect in topological metals. *Phys. Rev. B* **96**, 041110 (2017).

18. Liu, E., Sun, Y., Kumar, N., Muechler, L., Sun, A., and Jiao, L. et al., Giant anomalous Hall effect in a ferromagnetic kagome-lattice semimetal. *Nat. Phys.* **14**, 1125–1131 (2018).
19. Nakatsuji, S., Kiyohara, N., and Higo, T. Large anomalous Hall effect in a non-collinear antiferromagnet at room temperature. *Nature* **527**, 212–215 (2015).
20. von Neumann, V. J., and Wigner, E., Uber merkwürdige diskrete Eigenwerte. *Phys. Z.* **30**, 291-293 (1929).
21. Murakami, S., Iso, S., Avishai, Y., Onoda, M., and Nagaosa, N. Tuning phase transition between quantum spin Hall and ordinary insulating phases. *Phys. Rev. B* **76**, 205304 (2007).
22. Wilde, M. A., Dodenhöft, M., Niedermayr, A., Bauer, A., Hirschmann, M. M., and Alpin, K. et al., Symmetry-enforced topological nodal planes at the Fermi surface of a chiral magnet. *Nature* **594**, 374–379 (2021).
23. Kunschuh, S., Gmitra, M., and Fabian, J. Tight-binding theory of the spin-orbit coupling in graphene. *Phys. Rev. B* **82**, 245412 (2010).
24. Sichau, J., Prada, M., Anlauf, T., Lyon, T. J., Bosnjak, B., Tiemann, L., and Blick, R. H. Resonance Microwave Measurements of an Intrinsic Spin-Orbit Coupling Gap in Graphene: A Possible Indication of a Topological State. *Phys. Rev. Lett.* **122**, 046403 (2019).
25. Yuan, Q. Q., Zhou, L., Rao, Z. C., Tian, S., Zhao, W. M., and Xue, C. L. et al., Quasiparticle interference evidence of the topological Fermi arc states in chiral fermionic semimetal CoSi. *Sci. Adv.* **5**, eaaw9485 (2019).

26. Sanchez, D. S., Belopolski, I., Cochran, T. A., Xu, X., Yin, J.-X., and Chang, G. Q. et al., Topological chiral crystals with helicoid-arc quantum states. *Nature* **567**, 500–505 (2019).
27. Fang, C., Gilbert, M. J., Dai, X., and Bernevig, B. A. Multi-Weyl topological semimetals stabilized by point group symmetry. *Phys. Rev. Lett.* **108**, 266802 (2012).
28. Moll, P. J. W. Focused Ion Beam Microstructuring of Quantum Matter. *Annu. Rev. Condens. Matter Phys.* **9**, 147-162 (2018).
29. Xu, X., Wang, X., Cochran, T. A., Sanchez, D. S., Chang, G., and Belopolski, I. et al., Crystal growth and quantum oscillations in the topological chiral semimetal CoSi. *Phys. Rev. B* **100**, 045104 (2019).
30. Wu, D. S., Mi, Z. Y., Li, Y. J., Wu, W., Li, P. L., and Song, Y. T. et al., Single Crystal Growth and Magnetoresistivity of Topological Semimetal CoSi. *Chin. Phys. Lett.* **36**, 077102 (2019).
31. Wang, H., Xu, S., Lu, X. Q., Wang, X. Y., Zeng, X. Y., and Lin, J. F. et al., de Haas–van Alphen quantum oscillations and electronic structure in the large-Chern-number topological chiral semimetal CoSi. *Phys. Rev. B* **102**, 115129 (2020).
32. Huber, N., Alpin, K., Causer, G. L., Worch, L., Bauer, A., Benka, G. et al., Network of topological nodal planes, multifold degeneracies, and Weyl points in CoSi. *arXiv: 2107.02820* (2021).
33. Blount, E. I., Bloch Electrons in a Magnetic Field. *Phys. Rev.* **126**, 1636-1653 (1962).
34. Helm, T., Kartsovnik, M. V., Proust, C., Vignolle, B., Putzke, C., Kampert, E. et al., Correlation between Fermi surface transformations and superconductivity in the electron-doped high- $T_c$  superconductor  $\text{Nd}_{2-x}\text{Ce}_x\text{CuO}_4$ . *Phys. Rev. B* **92**, 094501 (2015).

35. Honold, M. M., Harrison, N., Nam, M.-S., Singleton, J., Mielke, C. H., Kurmoo, M., and Day, P. Magnetic breakdown in the high-field phase of the organic conductor  $\alpha$ -(BEDT-TTF)<sub>2</sub>KHg(SCN)<sub>4</sub>. *Synth. Met.* **103**, 2093-2094 (1999).
36. Pezzini, S., van Delft, M. R., Schoop, L. M., Lotsch, B. V., Carrington, A., Katsnelson, M. I., Hussey, N. E., and Wiedmann, S. et al., Unconventional mass enhancement around the Dirac nodal loop in ZrSiS. *Nat. Phys.* **14**, 178–183 (2017).
37. Bachmann, M. D., Ferguson, G. M., Theuss, F., Meng, T., Putzke, C., Helm, T. et al., Spatial control of heavy-fermion superconductivity in CeIrIn<sub>5</sub>. *Science* **366**, 221-226 (2019).
38. Sun, Y., Zhang, Y., Liu, C. X., Felser, C., and Yan, B. Dirac nodal lines and induced spin Hall effect in metallic rutile oxides. *Phys. Rev. B* **95**, 235104 (2017).
39. Sun, Y., Zhang, Y., Felser, C., and Yan, B. Strong intrinsic spin Hall effect in the TaAs family of Weyl semimetals. *Phys. Rev. Lett.* **117**, 146403 (2016).
40. Sodemann, I. and Fu, L. Quantum Nonlinear Hall Effect Induced by Berry Curvature Dipole in Time-Reversal Invariant Materials. *Phys. Rev. Lett.* **115**, 216806 (2015).
41. Yu, Z. M., Zhang, Z. Y., Liu, G. B., Wu, W. K., Li, X. P., and Zhang, R. W. et al., Encyclopedia of emergent particles in three-dimensional crystals. *Sci. Bull.* **67**, 375-380 (2022).
42. Winkler, R., *Spin-Orbit Coupling Effects in Two-Dimensional Electron and Hole Systems*. Springer Tracts in Modern Physics (2021).
43. Yao, M., Manna, K., Yang, Q., Fedorov, A., Voroshnin, V., and Schwarze, B. V. et al., Observation of giant spin-split Fermi-arc with maximal Chern number in the chiral topological semimetal PtGa. *Nat. Comms.* **11**, 2033 (2020).

44. Ma, J. Z., Wu, Q. S., Song, M., Zhang, S.-N., Guedes, E. B. and Ekahana, S. A. et al., Observation of a singular Weyl point surrounded by charged nodal walls in PtGa. *Nat. Comms.* **12**, 3994 (2021).
45. Xu, S., Zhou, L., Wang, X.Y., Wang, H., Lin, J.F., Zeng, X.Y., Cheng, P., Weng, H. and Xia, T.L. Quantum Oscillations and Electronic Structure in the Large-Chern-Number Topological Chiral Semimetal PtGa. *Chin. Phys. Lett.* **37**, 107504 (2020).
46. Schröter, N. B. M., Pei, D., Vergniory, M. G., Sun, Y, Manna, K., and de Juan, F. et al., Chiral topological semimetal with multifold band crossings and long Fermi arcs. *Nat. Phys.* **15**, 759–765 (2019).
47. Schröter, N. B. M., Stolz, S., Manna, K., de Juan, F., Vergniory, M. G., and Krieger J. A. et al., Observation and control of maximal Chern numbers in a chiral topological semimetal. *Science* **369**, 179-183 (2020).
48. Sessi, P., Feng-ren, F., Küster, F., Manna, K., and Vergniory, M. G. et al., Handedness-dependent quasiparticle interference in the two enantiomers of the topological chiral semimetal PdGa. *Nat. Comms.* **11**, 3507 (2020).
49. Chang, G., Xu, S. Y., Wieder, B. J., Sanchez, D. S., Huang, S. M., and Belopolski, I. et al., Unconventional chiral fermions and large topological Fermi arcs in RhSi. *Phys. Rev. Lett.* **119**, 206401 (2017).
50. Rees, D., Manna, K., Lu, B., Morimoto, T., Borrmann, H., and Felser, C. et al., Helicity-dependent photocurrents in the chiral Weyl semimetal RhSi. *Sci. Adv.* **6**, eaba0509 (2020).
51. Mühlbauer, S., Binz, B., Jonietz, F., Pfleiderer, C., Rosch, A., and Neubauer, A. et al., Skyrmion Lattice in a Chiral Magnet. *Science* **323**, 915-919 (2009).

52. Bradlyn, B., Elcoro, L., Cano, J., Vergniory, M., Wang, Z., Felser, C., Aroyo, M., and Bernevig, B. A. Topological quantum chemistry. *Nature* **547**, 298–305 (2017).
53. Zhang, T., Jiang, Y., Song, Z., Huang, H., He, Y., Fang, Z., Weng, H., and Fang, C. Catalogue of topological electronic materials. *Nature* **566**, 475–479 (2019).
54. Vergniory, M. G., Elcoro, L., Felser, C., Bernevig, B. A., and Wang, Z. A complete catalogue of high-quality topological materials. *Nature* **566**, 480–485 (2019).
55. Tang, F., Po, H. C., Vishwanath, A., and Wan, X. G. Comprehensive search for topological materials using symmetry indicators. *Nature* **566**, 486–489 (2019).

1 **Supplementary materials for ”Quasi-symmetry protected topology in a**  
2 **semi-metal”**

3 Chunyu Guo\*,<sup>1</sup> Lunhui Hu\*,<sup>2</sup> Carsten Putzke,<sup>1,3</sup> Jonas Diaz,<sup>1</sup> Xiangwei Huang,<sup>1</sup>  
4 Kaustuv Manna,<sup>4,5</sup> Feng-Ren Fan,<sup>4</sup> Chandra Shekhar,<sup>4</sup> Yan Sun,<sup>4</sup> Claudia  
5 Felser,<sup>4</sup> Chaoxing Liu<sup>†,2,6</sup> B. Andrei Bernevig<sup>†,6,7,8</sup> and Philip J. W. Moll<sup>†1</sup>

6 <sup>1</sup>*Laboratory of Quantum Materials (QMAT), Institute of Materials (IMX),*  
7 *École Polytechnique Fédérale de Lausanne (EPFL), CH-1015 Lausanne, Switzerland*

8 <sup>2</sup>*Department of Physics, The Pennsylvania State University, University Park, PA, USA*

9 <sup>3</sup>*Max Planck Institute for the Structure and Dynamics of Matter, 22761 Hamburg, Germany*

10 <sup>4</sup>*Max Planck Institute for Chemical Physics of Solids, 01187 Dresden, Germany*

11 <sup>5</sup>*Department of Physics, Indian Institute of Technology Delhi, New Delhi 110016, India*

12 <sup>6</sup>*Department of Physics, Princeton University, Princeton, New Jersey 08544, USA*

13 <sup>7</sup>*Donostia International Physics Center,*

14 *P. Manuel de Lardizabal 4, 20018 Donostia-San Sebastian, Spain*

15 <sup>8</sup>*IKERBASQUE, Basque Foundation for Science, Bilbao, Spain*

16 (Dated: June 1, 2022)



## 17 I. EXPERIMENTAL AND THEORETICAL METHODS

### 18 A. Single crystal growth

19 CoSi single crystals were grown in Te-flux. The high purity starting materials Co (99.95%,  
20 Alfa Aesar), Si (99.999%, Chempur) and Te (99.9999%, Alfa Aesar) were mixed in the molar  
21 ratio of 1:1:20. All materials were kept in a cylindrical alumina crucible and sealed in a quartz  
22 tube. The entire assembly was heated to 1050 °C at a rate of 100 °C/h, and held there for for 15 h to  
23 ensure a homogeneous mixture. Successively, the sample was cooled to 700 °C at a rate of 2 °C/h,  
24 and extra Te-flux was removed by centrifugation at 700 °C. High quality CoSi single crystals  
25 in the mm-range resulted from this growth protocol. These single crystals resemble octahedra,  
26 indicating a dominant growth along the [111] direction [Fig. S1 (a)]. The quality of the single-  
27 phase crystallinity was checked by Laue and single crystal X-Ray diffraction. The Laue diffraction  
28 pattern of CoSi matches well with the theoretically simulated one [Fig. S1 (b)], demonstrating high  
29 crystalline quality.

### 30 B. Focused-ion-beam (FIB) microstructuring

31  $100 \times 40 \times 2 \mu\text{m}$  thin slabs were cut out from a CoSi single crystal via a FEI Helios Plasma  
32 FIB using Xe-ions. The lamella was then transferred to a sapphire substrate ex-situ with a micro-  
33 manipulator and glued down with the red araldite epoxy. Afer that it was structured to the designed  
34 geometry with the Plasma FIB.

### 35 C. Details of ab-initio band structure calculation

36 Electronic band structures of CoSi were calculated by density functional theory (DFT) using the  
37 full-potential local-orbital code (FPLO)<sup>1</sup> with a localized atomic basis and full potential treatment  
38 (Fig. S2). The exchange and correlation energies were considered in the generalized gradient ap-  
39 proximation level<sup>2</sup>. To calculate the Fermi surface, we projected Bloch states onto high symmetric  
40 atomic-orbital-like Wannier functions and constructed tight-binding model Hamiltonian.

## 41 II. DETAILED ANALYSIS OF FERMI SURFACES AT R-POINT

### 42 A. Fermi surface Identity

43 Following the band character identification in band structure calculations [Fig. 2(d)] presented  
44 in the main manuscript, the four corresponding Fermi surfaces are also labelled as  $1^+$ ,  $1^-$ ,  $2^+$   
45 and  $2^-$  (Fig. S3). Here 1 and 2 denote the orbit character while +/- stand for the spin character.  
46 Note that the sizes of 1- and 2- Fermi surfaces are larger than their spin-opposite counterpart due  
47 to spin-orbit-coupling as discussed in Sec. II C. For the clarification we separate them into two  
48 pairs:  $1^+/2^+$  and  $1^-/2^-$ . Due to crystalline symmetry, these Fermi surfaces intersect exactly at the  
49 Brillouin zone boundary.

### 50 B. Slice-and-view of Fermi surfaces

51 To further demonstrate the Fermi surface geometry, the slice-and-view of the four Fermi sur-  
52 faces is displayed in Fig. S4. As slicing from the top to the bottom of the Fermi surfaces, the slice  
53 section changes from ellipsoidal to circular and then back to ellipsoidal. Note that the ellipsoids  
54 from the top and bottom slice are elongated along orthogonal directions. This orthogonality is  
55 generally true for all Fermi surfaces [Fig. S4 (a) and (b)]. The combination of all sliced orbits, as  
56 displayed in Fig. S4 (c), show both crossings at the high symmetry plane and crossings protected  
57 by quasi-symmetry.

58 The Fermi surface orbits with field applied along different directions are shown in Fig. S5 (b)  
59 which demonstrate the evolution of degeneracies at the Fermi surfaces. For all four field directions  
60 displayed, the Fermi surface orbits are intersecting at multiple k-points. Degeneracies occur at the  
61 Brillouin zone boundary are protected by crystalline symmetry, while the others located at low  
62 symmetry k-points are formed due to quasi-symmetry. These two different types of degeneracies  
63 are denoted with different colors on Fig. S5 (b). The momentum difference from R-point  $\Delta k$   
64 as a function of angle  $\phi$  with different applied field directions is presented in Fig. S5 (c) with  $\phi$   
65 defined in S5 (b). Two different types of degenerate points are marked with pink and blue circles  
66 respectively.

### 67 C. Influence of spin-orbit-coupling

68 In this section, we discuss the influence of spin-orbit-coupling (SOC) on band structure. With-  
69 out SOC, the spin degeneracy is preserved and therefore all bands are at least two-fold degenerate  
70 throughout the Brillouin zone. At the boundary of the Brillouin zone, the crystalline symmetry en-  
71 forces a four-fold band degeneracy, as revealed by the ab-initio band structure calculation [Fig. S6  
72 (a)]. If the SOC is included, spin degeneracy will be lifted therefore all bands are non-degenerate  
73 except either at the high symmetry planes or the quasi-symmetry protected planes [Fig. S4 (b)].  
74 This difference is exemplified for the Fermi surface orbits with different field directions. When  
75 the magnetic field is applied along [100] axis, the non-SOC orbits are four-fold degenerate [Fig.  
76 S6 (c)] while for SOC-included case the orbits are doubly degenerate [Fig. S6 (d)]. In the mean-  
77 time for  $B//[110]$  the non-SOC orbits are doubly degenerate except at the high symmetry lines  
78 [Fig. S6 (e)], while for SOC-included case the four orbits are almost non-degenerate [Fig. S6 (f)]  
79 yet displays a complex intersecting pattern with degeneracies occur only at certain k-point. The  
80 three-dimensional (3D) view of the Fermi surfaces for both non-SOC and SOC-included cases are  
81 displayed in Fig. S6 (g) and (h) respectively.

### 82 III. NEAR-DEGENERACY DUE TO QUASI-SYMMETRY

83 To display the near-degeneracy due to quasi-symmetries, Fermi surfaces with different orbital  
84 and spin characters, namely  $1^+/2^-$  and  $1^-/2^+$ , are paired up (Fig. S7). The intersections between  
85 the Fermi surfaces form four rings for each pair and therefore eight rings in total. As the position  
86 of the degenerate rings strongly depend on the size and shape of the Fermi surfaces, by tuning the  
87 Fermi level of the system, the degenerate rings are reshaped and relocated in the Brillouin zone  
88 (Fig. S8). When the Fermi level is tuned to the type-II Weyl point located along the R to  $\Gamma$  line, the  
89 degenerate rings shrink to eight singular Weyl points at the Fermi surface and vanish with further  
90 reducing the Fermi level. By combining all degenerate rings at different Fermi energy, degenerate  
91 planes protected by the quasi-symmetry is constructed (Fig. S9). The degenerate planes contain  
92 eight different planes which are all symmetrically related (Fig. S10).

## 93 IV. SHUBNIKOV–DE HAAS OSCILLATION MEASUREMENTS OF COSI

94 Four microstructure devices are fabricated by focused-ion-beam technique in order to perform  
95 Shubnikov–de Haas (SdH) oscillation measurements with field applied along different directions.  
96 For device-1, a microbar along [100] axis with a cross section area of 6 by 6  $\mu m^2$  is fabricated  
97 [Fig. S11 (a)], and the quantum oscillations are measured with magnetic field rotate within the  
98 (100) plane [Fig. S11 (b)]. This ensures the magnetic field direction is always perpendicular to  
99 the current direction which eliminates the possible influence of longitudinal magnetotransport.  
100 The SdH oscillations are measured with a 10-degree-step rotation starting from [001] axis [Fig.  
101 S11 (c)], and the corresponding angle-dependent fast-Fourier-transformation (FFT) spectrum is  
102 displayed in Fig. S11 (d). In order to demonstrate the consistency of our analysis, we have also  
103 analyzed the angular dependence of second harmonic oscillation frequencies which can be nicely  
104 described by the theoretical prediction as well (Fig. S12).

105 To further investigate the Fermiology of CoSi, another micro-bar along  $[1\bar{1}0]$  axis is fabricated  
106 [Fig. S13 (a)]. The magnetic field is therefore rotated from [001] to [110] axis [Fig. S13 (b)].  
107 Angle-dependent SdH oscillations and corresponding FFT spectrum are displayed in Fig. S13 (c)  
108 and (d) respectively. The angular dependence of oscillation frequency is summarized in Fig. S13  
109 (e). Similarly, the experimental results match well with the theoretical prediction, which further  
110 demonstrates the importance of quasi-symmetry in CoSi.

### 111 A. Determination of cyclotron mass

112 To accurately determine the corresponding cyclotron mass of the Fermi surfaces, we have per-  
113 formed SdH oscillation measurements of device-1 down to 50 mK [Fig. 3 (a)] with both magnetic  
114 field and current applied along [100] direction. The temperature dependence of the oscillations fol-  
115 lows well the Lifshitz-Kosevich form, leading to a low cyclotron effective mass of  $m_c \approx 0.84 m_e$   
116 (Fig. S14) which is consistent with the previous report<sup>7,8</sup>.

### 117 B. Analysis of quantum oscillation spectrum under tensile strain along [111] axis

118 In the main manuscript, we explained how tensile strain breaks crystalline symmetry of CoSi  
119 which leads to the observation of additional quantum oscillation with different frequencies. To fur-  
120 ther demonstrate the relation between strain-induced additional oscillation frequencies and crys-

121 talline symmetry breaking, here we presented detailed analysis of SdH oscillations of device-3  
122 measured at  $T = 50$  mK with a tensile strain along [111] direction(Fig. S15). Similar to the  
123 tensile strain approximately along [110] axis, additional satellite peaks around the main frequen-  
124 cies are also clearly resolved. By calculating the additional orbital area generated by breaking  
125 either crystalline or quasi-symmetry, we confirmed that the experimental results can only be de-  
126 scribed by the quasi-symmetry-preserved scenario which, on the other hand, further demonstrates  
127 the stability of quasi-symmetry against strain-induced crystalline symmetry breaking.

### 128 C. Gaussian-type multi-peak fit of FFT spectrum

129 In order to accurately determine the position and relative size of the satellite peaks induced  
130 by tensile strain along [110], we performed both 3-peak and 5-peak Gaussian fit to the the FFT  
131 spectrum presented in Fig.4 (e). 3-peak Gaussian fit [Fig. S16 (a)] describes the experimental  
132 spectrum reasonably well which clearly demonstrates the existence of two satellite peaks. The fre-  
133 quency difference between the main and satellite peaks always stay around  $32 T$  for all principle  
134 frequencies and their higher harmonics. Slight discrepancy between the spectrum of third har-  
135 monic oscillations and the 3-peak Gaussian fit is mainly due to its much reduced amplitude which  
136 is comparable to the noise floor of the FFT analysis. 5-peak Gaussian fit for both first and second  
137 harmonic spectrum is almost identical to the 3-peak fit since the two additional peaks are almost  
138 negligible. While for the third harmonic spectrum, although the fitting quality is improved with  
139 including the two additional peaks, they do not match with the theoretical prediction of crystalline-  
140 symmetry-preserved scenario. These results rigorously demonstrate that strain-induced crystalline  
141 symmetry breaking is the origin of the satellite peaks in the FFT spectrum. To note that since these  
142 additional frequencies rely on the magnetic breakdown tunnelling at the symmetry breaking point,  
143 their amplitudes are much smaller compared to the principle ones. Therefore it is necessary to  
144 perform the measurement down to  $T = 50$  mK as to magnify the quantum oscillation amplitude  
145 as much as possible. In the mean time, the breakdown pattern may also be related to the slight  
146 misalignment of strain direction from [110] which we discussed in details in Sec. VII E.

147 In comparison, for strain along [111] direction the first harmonic FFT spectrum can also be  
148 well described by a 3-peak Gaussian fit (Fig. S17). Here the amplitude difference between the two  
149 different satellite peaks is possibly due to the slight strain inhomogeneity along the microstructure.  
150 For the second harmonic spectrum since the satellite peak height is again close to the FFT noise

151 floor, the 3-peak Gaussian fit displays limited fitting quality which is improved by including two  
 152 additional peaks in the 5-peak Gaussian fit. Similar to the [110] case, since the included additional  
 153 peaks are distinct from the expected ones for crystalline-symmetry-preserved case, they are most  
 154 likely due to the limited resolution of FFT analysis.

## 155 V. CALCULATION OF MAGNETIC BREAKDOWN FIELD AND CORRESPONDING CYCLOTRON 156 MASS

### 157 A. Calculation of magnetic breakdown field

158 Theoretically, the magnetic breakdown probability is defined as<sup>3</sup>:

$$P = e^{-H_0/H} \quad (\text{S1})$$

159 where  $H_0$  is the magnetic breakdown field given by:

$$H_0 = \frac{\pi}{4\hbar e} \frac{\Delta^2}{v_{\parallel} v_{\perp}} \quad (\text{S2})$$

160 here  $v_{\parallel}$  and  $v_{\perp}$  stand for the Fermi velocity along two in-plane directions perpendicular to the mag-  
 161 netic field. For example, with field applied along [110] axis,  $v_{\parallel}$  is the Fermi velocity along [001]  
 162 axis while  $v_{\perp}$  stands for Fermi velocity along  $[1\bar{1}0]$  direction. From band structure calculation we  
 163 obtained:

$$v_{\parallel} = 2.11 \times 10^5 \text{ m/s}, \quad v_{\perp} = 2.64 \times 10^5 \text{ m/s} \quad (\text{S3})$$

164 Meanwhile the breakdown gap  $\Delta \approx 2$  meV as presented in Fig. S19 (d). Therefore the magnetic  
 165 breakdown field is estimated to be around 0.11 T. Such a small magnetic breakdown field supports  
 166 the validity of our quasi-symmetry model. For other field orientations, the breakdown gap remains  
 167 smaller than 2 meV (Fig. S19) and the corresponding breakdown field  $H_0$  at any arbitrary field  
 168 direction is always smaller than 0.11 T. This means at the lowest field limit ( $B_c \approx 3$  T) where the  
 169 quantum oscillation starts to become observable, the breakdown transmission possibility is about  
 170 96.4%. This explains the clean quantum oscillation spectrum we observed (Fig. 3). This small  
 171 breakdown gap also implies the possibility of zero-field topological application above  $T = 20$  K  
 172 as the thermal broadening renders the breakdown gap transparent.

## B. Calculation of corresponding cyclotron mass of the breakdown orbits

Based on DFT calculations one can easily obtain the expected cyclotron mass  $m_c \approx 0.78 m_e$  for all four pockets with field applied along [100] direction, which is consistent with the experimental result of  $m_c \approx 0.84 m_e$ . Note that in semi-classical theory<sup>4</sup>, if the breakdown orbit consists with two original orbits as shown in Fig. S18(a), the cyclotron mass of the breakdown orbit can be estimated by directly adding the masses of individual pockets. However this simple scenario is not applicable for CoSi where the intersection of different original orbits results in two instead of only one breakdown orbits. Therefore based on semi-classical theory one can deduce that the sum of cyclotron mass of the two original/breakdown orbits should be similar. This means the original and breakdown orbit should have similar cyclotron mass value  $m_c \approx 0.78m_e$  which is consistent with the experimental results. We can also directly calculate the cyclotron mass of the breakdown orbits in CoSi assuming the quasi-symmetry protected degeneracy is gapless. The calculation yields a similar cyclotron mass value around  $0.77 m_e$ , which again matches well with the experimental results.

## VI. GENERALITY OF QUASI-SYMMETRY

As the quasi-symmetry originates from the  $\mathbf{k} \cdot \mathbf{p}$ -type expansion of effective model, we would expect it is a general property that exists in materials with the same crystal structure. To demonstrate this point, we studied the electronic band structure of three different compounds, PtAl, PtGa and RhSi, which share the same crystal structure as CoSi. We notice that the band structure of RhSi is almost identical to that of CoSi with an electron pocket around R point and a hole pocket around  $\Gamma$  point, while for PtAl and PtGa, the electron pockets exist for both  $\Gamma$  and R points and the additional hole pockets appear around the M points. The electron Fermi pockets around the R point are all similar and described by the same effective model for all these compounds and as shown in Fig. S20, these Fermi surfaces in the [110] plane display both crystalline-symmetry-protected exact degeneracies and quasi-symmetry-protected near degeneracies, similar to CoSi. Since the quasi-symmetry is approximate, a small gap is expected for the near degeneracies, as labelled by blue dots in Fig. S20, and the sizes of these gaps vary at the Fermi surfaces for different materials. We find this gap is extremely small also for RhSi, but a bit larger for PtAl and PtGa, which depends on the material details. Nevertheless, our calculations here demonstrate that the

202 scenario of quasi-symmetry can generally be applied to all these compounds.



203 **VII. THEORETICAL MODELLING**

204 **A. Space group 198 of CoSi**

205 The chiral crystal CoSi has a space group 198 (SG198), which can be generated by

$$S_{2x} = \{C_{2x}|\frac{1}{2}\frac{1}{2}0\}, C_3 = \{C_{3,(111)}|000\}, \quad (\text{S4})$$

206 in addition to the translation sub-group<sup>5</sup>. Hereafter, the Seitz notation is taken for the non-  
 207 symmorphic symmetry operations, i.e., a point group operation  $\mathcal{O}$  followed by a translation  $\mathbf{v} =$   
 208  $v_i \mathbf{t}_i$ , labeled as  $\hat{\mathcal{O}} = \{\mathcal{O}|\mathbf{v}\}$  or  $\hat{\mathcal{O}} = \{\mathcal{O}|v_1 v_2 v_3\}$ , with  $\mathbf{t}_i$  ( $i = 1, 2, 3$ ) representing three basis  
 209 vectors for a Bravais lattice in three dimensions [see Fig. 2(a) in the main text] The reciprocal  
 210 space lattice vectors are generated by  $\mathbf{g}_i$ , where  $\mathbf{g}_i \cdot \mathbf{t}_j = 2\pi\delta_{ij}$ . The rules for multiplication and  
 211 inversion are defined as

$$\{\mathcal{O}_2|\mathbf{v}_2\}\{\mathcal{O}_1|\mathbf{v}_1\} = \{\mathcal{O}_2\mathcal{O}_1|\mathbf{v}_2 + \mathcal{O}_2\mathbf{v}_1\}, \quad (\text{S5})$$

$$\{\mathcal{O}|\mathbf{v}\}^{-1} = \{\mathcal{O}^{-1}|\mathbf{v}\}. \quad (\text{S6})$$

212 The  $S_{2y} = \{C_{2y}|0\frac{1}{2}\frac{1}{2}\}$  symmetry can be generated by

$$S_{2y} = C_3^{-1}S_{2x}C_3, \quad (\text{S7})$$

213 where we take the convention for  $C_{3,(111)} : (x, y, z) \rightarrow (y, z, x)$ , leading to  $C_{2y} = C_{3,(111)}^{-1}C_{2x}$   
 214  $C_{3,(111)}$ . Likewise, the  $S_{2z}$  symmetry can be given by the combination of  $S_{2x}$ ,  $S_{2y}$  and the transla-  
 215 tion operator  $E_{\mathbf{v}} = \{E|\mathbf{v}\}$ ,

$$S_{2x}S_{2y} = \{E|00\bar{1}\}S_{2z} \triangleq E_{00\bar{1}}S_{2z}. \quad (\text{S8})$$

216 Similar to the MnSi in Ref. [6], the symmetry-enforced nodal planes (high symmetry planes)  
 217 also exist for CoSi. On these high-symmetry planes, the two-fold degeneracies are protected by the  
 218 combined anti-unitary symmetries,  $S_{2x}\mathcal{T}$ ,  $S_{2y}\mathcal{T}$  and  $S_{2z}\mathcal{T}$ , where  $\mathcal{T}$  is the time-reversal operator.  
 219 For spinless fermions,  $\mathcal{T} = \mathcal{K}$  with the complex conjugate  $\mathcal{K}$ , while for the spin-1/2 fermions,

220  $\mathcal{T} = i s_y \mathcal{K}$  with  $s_y$  the Pauli matrix acting on the spin subspace. These operations transform the  
 221 Hamiltonian as

$$(S_{2x}\mathcal{T})^\dagger \mathcal{H}(k_x, k_y, k_z) (S_{2x}\mathcal{T}) = \mathcal{H}(-k_x, k_y, k_z), \quad (\text{S9})$$

$$(S_{2y}\mathcal{T})^\dagger \mathcal{H}(k_x, k_y, k_z) (S_{2y}\mathcal{T}) = \mathcal{H}(k_x, -k_y, k_z), \quad (\text{S10})$$

$$(S_{2z}\mathcal{T})^\dagger \mathcal{H}(k_x, k_y, k_z) (S_{2z}\mathcal{T}) = \mathcal{H}(k_x, k_y, -k_z). \quad (\text{S11})$$

222 It indicates that  $[S_{2x}\mathcal{T}, \mathcal{H}(k_x = 0, \pi, k_y, k_z)] = 0$  for the  $k_x = 0, \pi$  planes. Likewise, the  $S_{2y}\mathcal{T}$ -  
 223 invariant ( $S_{2z}\mathcal{T}$ -invariant) planes are  $k_y = 0, \pi$  ( $k_z = 0, \pi$ ). Moreover, we act the operators  $S_{2x}\mathcal{T}$ ,  
 224  $S_{2y}\mathcal{T}$  and  $S_{2z}\mathcal{T}$  on the Bloch wave functions at  $\mathbf{k}$  and find  $(S_{2x}\mathcal{T})^2 = (S_{2y}\mathcal{T})^2 = (S_{2z}\mathcal{T})^2 = -1$   
 225 at the  $k_i = \pi$  plane. Thus,  $S_{2x}\mathcal{T}$ ,  $S_{2y}\mathcal{T}$  and  $S_{2z}\mathcal{T}$  behave as the time reversal operator for spinful  
 226 fermions, and the two-fold degeneracy on the  $k_{x,y,z} = \pi$ -plane can be guaranteed by these anti-  
 227 unitary symmetries, similar to the Kramers' theorem, as depicted in Fig. S4(c).

## 228 B. The effective model Hamiltonian around the $R$ -point

229 In this section, we construct the effective  $\mathbf{k} \cdot \mathbf{p}$  Hamiltonian around the  $R$ -point ( $\mathbf{k}_R = (\pi, \pi, \pi)$ ),  
 230 and fit parameters for the  $\mathbf{k} \cdot \mathbf{p}$  bands with the density-functional-theory (DFT) bands.

231 We first consider the commutation relations of the symmetry operators  $S_{2x}$ ,  $S_{2y}$  and  $\mathcal{T}$  in SG198  
 232 for spinless fermions at  $R$ , given by

$$\{S_{2x}, S_{2y}\} = 0, [\mathcal{T}, S_{2x}] = [\mathcal{T}, S_{2y}] = 0 \text{ and } (S_{2x}\mathcal{T})^2 = (S_{2y}\mathcal{T})^2 = -1. \quad (\text{S12})$$

233 For a common eigen-state  $|\Psi\rangle$  of  $S_{2x}$  with eigenvalue  $\lambda$  and the Hamiltonian, the  $S_{2x}$ -  
 234 eigenvalues of the states  $S_{2y}|\Psi\rangle$ ,  $\mathcal{T}|\Psi\rangle$  and  $S_{2y}\mathcal{T}|\Psi\rangle$  are given in the following table,

	$ \Psi\rangle$	$S_{2y} \Psi\rangle$	$\mathcal{T} \Psi\rangle$	$S_{2y}\mathcal{T} \Psi\rangle$
235 $S_{2x}$	$\lambda$	$-\lambda$	$\lambda^* = -\lambda$	$-\lambda^* = \lambda$

236 from which we find  $|\Psi\rangle, S_{2y}\mathcal{T}|\Psi\rangle$  and  $S_{2y}|\Psi\rangle, \mathcal{T}|\Psi\rangle$  carry opposite  $S_{2x}$ -eigenvalues. Here  
 237 we have used the fact that  $\lambda$  is a purely imaginary number due to  $S_{2x}^2 = -1$ . Furthermore,  
 238 since  $(S_{2y}\mathcal{T})^2 = -1$  and  $S_{2y}\mathcal{T}$  is an anti-unitary symmetry operator,  $\langle\Psi|S_{2y}\mathcal{T}|\Psi\rangle = 0$ , which  
 239 means the states  $|\Psi\rangle$  and  $S_{2y}\mathcal{T}|\Psi\rangle$  ( $S_{2y}|\Psi\rangle$  and  $\mathcal{T}|\Psi\rangle$ ) are orthogonal to each other. Thus,

240  $\{|\Psi\rangle, S_{2y}|\Psi\rangle, \mathcal{T}|\Psi\rangle, S_{2y}\mathcal{T}|\Psi\rangle\}$  are four independent degenerate eigen-states of the Hamiltonian.  
 241 This proves all the eigen-states of the Hamiltonian at the R-point are four-fold degenerate (without  
 242 spin), and thus supports the discussions in the main text above Eq. (1).

243 Next we will construct the effective model on the four-fold degenerate states based on the  
 244 symmetry argument. Let us choose  $G_1, G_2$  and  $G_3$  to be the matrix representations for the  $S_{2x},$   
 245  $S_{2y},$  and  $C_3,$  respectively. Without spin, these matrix representations need to satisfy the relations

$$G_3^3 = 1, G_1^2 = G_2^2 = -1, G_1G_2 = -G_2G_1, G_3^{-1}G_1G_3 = G_2, G_3^{-1}G_2G_3 = -G_1G_2. \quad (\text{S13})$$

246 Moreover, all of them commute with time-reversal symmetry,  $[G_1, \mathcal{T}] = [G_2, \mathcal{T}] = [G_3, \mathcal{T}] = 0$   
 247 for  $\mathcal{T} = K$ . Thus, one can construct the 4D irreducible representation matrices for  $G_1, G_2$  and  $G_3$   
 248 as

$$G_3 = \begin{pmatrix} 1 & 0 & 0 & 0 \\ 0 & 0 & -1 & 0 \\ 0 & 0 & 0 & 1 \\ 0 & -1 & 0 & 0 \end{pmatrix}, G_1 = \begin{pmatrix} 0 & 0 & 1 & 0 \\ 0 & 0 & 0 & 1 \\ -1 & 0 & 0 & 0 \\ 0 & -1 & 0 & 0 \end{pmatrix} = i\sigma_y\tau_0, G_2 = \begin{pmatrix} 0 & 0 & 0 & 1 \\ 0 & 0 & -1 & 0 \\ 0 & 1 & 0 & 0 \\ -1 & 0 & 0 & 0 \end{pmatrix} = i\sigma_x\tau_y. \quad (\text{S14})$$

249 Here we have chosen two sets of Pauli matrices  $\sigma$  and  $\tau$  to rewrite the four by four matrices.  
 250 Based on the above three transformation matrices for  $G_1, G_2$  and  $G_3$  and time reversal operator  
 251  $\mathcal{T} = \mathcal{K}$ , we can construct the effective Hamiltonian around the R-point as (without spin)

$$\mathcal{H}_{non-soc}(\mathbf{k}) = \mathcal{H}_0(\mathbf{k}) + \mathcal{H}_{k^2}(\mathbf{k}), \quad (\text{S15})$$

252 where the the leading order Hamiltonian reads

$$\mathcal{H}_0(\mathbf{k}) = C_0\sigma_0\tau_0 + A_1(k_x\sigma_y\tau_0 + k_y\sigma_x\tau_y - k_z\sigma_z\tau_y), \quad (\text{S16})$$

253 and the  $k^2$ -order Hamiltonian is

$$\begin{aligned} \mathcal{H}_{k^2}(\mathbf{k}) = & B_1k^2\sigma_0\tau_0 + C_1(k_xk_y\sigma_z\tau_0 + k_yk_z\sigma_0\tau_z + k_xk_z\sigma_z\tau_z) + C_2(k_xk_y\sigma_x\tau_x \\ & - k_yk_z\sigma_0\tau_x + k_xk_z\sigma_x\tau_0) + C_3(k_xk_y\sigma_x\tau_z - k_yk_z\sigma_y\tau_y - k_xk_z\sigma_z\tau_x), \end{aligned} \quad (\text{S17})$$

254 with  $C_0, A_1, B_1, C_1, C_2, C_3$  material-dependent parameters and  $k = \sqrt{k_x^2 + k_y^2 + k_z^2}$ .

255 Next we will include spin-orbit coupling into the Hamiltonian. To do that, we note that spin is  
 256 a pseudo-vector and behaves exactly the same as a vector due to the lack of inversion, mirror or  
 257 other roto-inversion symmetries for a chiral crystal. Correspondingly, we just need to replace the  
 258 momentum  $\mathbf{k}$  by the Pauli matrices  $\mathbf{s}$  of the electron spin to get the effective spin-orbit coupling,  
 259 which is written as

$$\mathcal{H}_{soc} = \lambda_0(s_x\sigma_y\tau_0 + s_y\sigma_x\tau_y - s_z\sigma_z\tau_y), \quad (\text{S18})$$

260 up to the first order in spin, with the spin-orbit coupling parameter  $\lambda_0$ . The full Hamiltonian is  
 261 given by

$$\mathcal{H}_R(\mathbf{k}) = \mathcal{H}_{non-soc} \otimes s_0 + \mathcal{H}_{soc}. \quad (\text{S19})$$

262 For  $\lambda_0 = 0$ , one can check that the Hamiltonian  $\mathcal{H}_R(\mathbf{k})$  has a 8-fold degeneracy at  $R$ -point  
 263 ( $\mathbf{k} = 0$ ). Once the spin-orbit coupling is turned on, the 8-fold degeneracy at  $R$ -point is split into  
 264 a 6-fold (energy  $\lambda_0$ ) and a 2-fold (energy  $-3\lambda_0$ ). From the DFT calculation [see Fig. 2(c) in the  
 265 main text], we find that the 6-fold degenerated states have higher energy than that of the 2-fold  
 266 states, which implies  $\lambda_0 > 0$ .

267 The spin-independent Hamiltonian  $\mathcal{H}_0(\mathbf{k})$  is isotropic with the full rotation symmetry. To see  
 268 that, we could define the emergent angular momentum operators as

$$L_x = \frac{1}{2}\sigma_y\tau_0, \quad L_y = \frac{1}{2}\sigma_x\tau_y, \quad L_z = -\frac{1}{2}\sigma_z\tau_y, \quad (\text{S20})$$

269 which satisfies the commutation relation  $[L_i, L_j] = i\epsilon_{ijk}L_k$  with Levi-Civita symbol  $\epsilon_{ijk}$  and  
 270  $i = x, y, z$ . Therefore,  $\mathcal{H}_0(\mathbf{k})$  and  $\mathcal{H}_{soc}$  can be re-written as

$$\mathcal{H}_0(\mathbf{k}) = C_0\sigma_0\tau_0 + 2A_1(\mathbf{k} \cdot \mathbf{L}), \quad (\text{S21})$$

$$\mathcal{H}_{soc} = 2\lambda_0(\mathbf{s} \cdot \mathbf{L}), \quad (\text{S22})$$

271 which is shown in the Eq. (1) in the main text.  $\mathcal{H}_{k^2}(\mathbf{k})$  breaks the full rotational symmetry.  
 272 Moreover, we extract the parameters for the  $R$ -model in Eq. (S19) by fitting the DFT bands along  
 273 high symmetry lines, shown in Fig. S21. The parameters are

$$\begin{aligned}
C_0 &= -0.18 \text{ eV}, \lambda_0 = 0.0075 \text{ eV}, B_1 = 2.123 \text{ eV} \cdot \text{\AA}^2, A_1 = 0.853 \text{ eV} \cdot \text{\AA}, \\
C_1 &= -0.042 \text{ eV} \cdot \text{\AA}^2, C_2 = 0.546 \text{ eV} \cdot \text{\AA}^2, C_3 = 3.345 \text{ eV} \cdot \text{\AA}^2.
\end{aligned}
\tag{S23}$$

274 With this set of parameters, the bands near the  $R$ -point from the DFT are well reproduced by  
275 the effective model, shown in Fig. S21 (b).

### 276 C. The perturbation theory around the Fermi energy

277 According to the DFT calculation as well as the results from the effective  $R$  model in Eq. (S19),  
278 we find the near crossings which are consistent with the experimental results. A tiny gap ( $\sim 1$   
279 meV) for the near crossings is shown in Fig. S22 (a). To understand the origin of this tiny gap,  
280 we apply the perturbation theory to the model Hamiltonian (S19). We treat  $\mathcal{H}_0(\mathbf{k}) \otimes s_0$  as the  
281 unperturbed Hamiltonian and  $\mathcal{H}_{perb} = \mathcal{H}_{soc} + \mathcal{H}_{k^2}(\mathbf{k})$  as the perturbation Hamiltonian.

282 We first solve the eigen-problem of the Hamiltonian  $\mathcal{H}_0(\mathbf{k}) \otimes s_0$  and due to its full rota-  
283 tion symmetry, we choose the spherical coordinate for the momentum  $\mathbf{k} = (k_x, k_y, k_z) =$   
284  $k(\sin \theta \cos \phi, \sin \theta \sin \phi, \cos \theta)$ . The eigen-energies of  $\mathcal{H}_0(\mathbf{k}) \otimes s_0$  have two branches  $E_{\pm} =$   
285  $C_0 \pm A_1 k$  for which each branch has four-fold degeneracy. The four degenerate eigen-wave  
286 functions of the positive energy branch ( $E_+$ ) are given by

$$\begin{aligned}
|\Psi_{A+\uparrow}(\theta, \phi)\rangle &= |\Psi_{A+}(\theta, \phi)\rangle \otimes (1, 0)^T, \\
|\Psi_{B+\uparrow}(\theta, \phi)\rangle &= |\Psi_{B+}(\theta, \phi)\rangle \otimes (1, 0)^T, \\
|\Psi_{A+\downarrow}(\theta, \phi)\rangle &= |\Psi_{A+}(\theta, \phi)\rangle \otimes (0, 1)^T, \\
|\Psi_{B+\downarrow}(\theta, \phi)\rangle &= |\Psi_{B+}(\theta, \phi)\rangle \otimes (0, 1)^T,
\end{aligned}
\tag{S24}$$

287 where the spin-independent components are

$$|\Psi_{A+}(\theta, \phi)\rangle = \frac{1}{\sqrt{2}} (\cos \theta \cos \phi - i \sin \phi, -\cos \theta \sin \phi - i \cos \phi, 0, \sin \theta)^T, \tag{S25}$$

$$|\Psi_{B+}(\theta, \phi)\rangle = \frac{1}{\sqrt{2}} (-i \sin \theta \cos \phi, i \sin \theta \sin \phi, 1, i \cos \theta)^T, \tag{S26}$$

288 here we use  $\{A+, B+\}$  to label the two bands and  $\{\uparrow, \downarrow\}$  for the electron spin.

289 Then, we can project the angular momentum operator  $\mathbf{L}$  into the eigenstate subspace and find

$$\langle \Psi_{A+}(\theta, \phi) | \mathbf{L} | \Psi_{A+}(\theta, \phi) \rangle = \langle \Psi_{B+}(\theta, \phi) | \mathbf{L} | \Psi_{B+}(\theta, \phi) \rangle = \frac{\mathbf{k}}{2k}, \quad (\text{S27})$$

$$\langle \Psi_{A+}(\theta, \phi) | \mathbf{L} | \Psi_{B+}(\theta, \phi) \rangle = \langle \Psi_{B+}(\theta, \phi) | \mathbf{L} | \Psi_{A+}(\theta, \phi) \rangle = 0, \quad (\text{S28})$$

290 which means the emergent angular momentum operator  $\mathbf{L}$  is projected into the momentum  
 291 direction. Thus up to the first-order perturbation, the spin-orbit coupling term becomes the form  
 292 of  $\frac{\lambda_0}{k}(\mathbf{k} \cdot \mathbf{s}) \otimes I_{2 \times 2}$  after projecting into the eigen-state subspace,

$$|\Psi_{upper}\rangle = \{|\Psi_{A+\uparrow}(\theta, \phi)\rangle, |\Psi_{B+\uparrow}(\theta, \phi)\rangle, |\Psi_{A+\downarrow}(\theta, \phi)\rangle, |\Psi_{B+\downarrow}(\theta, \phi)\rangle\}, \quad (\text{S29})$$

293 which supports the discussions below Eq. (1) in the main text. The identity matrix  $I_{2 \times 2}$  indi-  
 294 cates that the first-order perturbation Hamiltonian of SOC does not couple different bands.

295 Next, we can apply the perturbation theory to consider the perturbation Hamiltonian  $\mathcal{H}_{perb}$  in  
 296 the subspace  $|\Psi_{upper}\rangle$  order by order. Up to the first-order perturbation, the perturbed Hamiltonian  
 297  $\mathcal{H}_P^{eff(1)}$  reads

$$\begin{aligned} \mathcal{H}_P^{eff(1)} &= (C_0 + B_1 k^2 + A_1 k) s_0 \omega_0 + \lambda_0 (\lambda_x s_x + \lambda_y s_y + \lambda_z s_z) \omega_0 \\ &+ \tilde{C} k^2 s_0 (d_x \omega_x + d_y \omega_y + d_z \omega_z). \end{aligned} \quad (\text{S30})$$

298 where  $\tilde{C} = C_1 - C_2 + C_3$ , and  $\omega_{x,y,z}$  are Pauli matrices for the  $\{A+, B+\}$  band subspace [+  
 299 means the upper four bands in Eq. (S24)]. The coefficient  $\lambda_{x,y,z}$  are defined as

$$(\lambda_x, \lambda_y, \lambda_z) = (\sin \theta \cos \phi, \sin \theta \sin \phi, \cos \theta) = \frac{\mathbf{k}}{|\mathbf{k}|}, \quad (\text{S31})$$

300 and  $d_{x,y,z}$  are given by

$$\begin{aligned} d_x &= \cos \theta \sin^2 \theta \sin \phi \cos \phi (\cos \phi + \sin \phi), \\ d_y &= \cos \theta \sin^2 \theta \sin \phi \cos \phi (\sin \theta + \cos \theta (\cos \phi - \sin \phi)), \\ d_z &= \sin^2 \theta \sin \phi \cos \phi (\cos^2 \theta + \sin \theta \cos \theta (-\cos \phi + \sin \phi)). \end{aligned} \quad (\text{S32})$$

301 The perturbation theory is valid only for  $A_1 k \gg \lambda_0$  and  $A_1 k \gg \frac{\sqrt{3}}{4} \tilde{C} k^2$ . With the parameters  
 302 used in this work [see Eq. (S23)], we can estimate the valid range of the momentum as

$$k_{min} < k < k_{max} \quad \Leftrightarrow \quad k_{min} = \frac{\lambda_0}{A_1} \approx 0.01 \text{ \AA}^{-1} \text{ and } k_{max} = \frac{4A_1}{\sqrt{3}\tilde{C}} \approx 0.7 \text{ \AA}^{-1}. \quad (\text{S33})$$

303 The eigen-energies of the effective Hamiltonian (S30) are given by

$$E_{\alpha\beta}(k, \theta, \phi) = C_0 + B_1 k^2 + A_1 k + \alpha \lambda_0 + \beta \frac{\sqrt{3}}{4} \tilde{C} k^2 |\sin 2\phi \sin 2\theta \sin \theta|, \quad (\text{S34})$$

304 where  $\alpha = \pm$  and  $\beta = \pm$ . These energy dispersions show the exact crossings in Fig. S22(b).  
 305 Note that  $\sin 2\phi \sin 2\theta \sin \theta = 4k_x k_y k_z / k^3$ , indicating the perturbation correction of  $\mathcal{H}_{k^2}$  breaks  
 306 the full rotational symmetry down to three-fold rotational symmetry.

307 Next we consider the second-order perturbation corrections, which open a tiny gap for the  
 308 emergent nodal lines [see Fig. S22(c)]. For the second-order perturbation, besides the eigen-state  
 309 basis set  $|\Psi_{upper}\rangle$  in Eq. (S24), we also need to take four negative energy ( $E_-$ ) eigen-states

$$|\Psi_{lower}\rangle = \{|\Psi_{A-\uparrow}(\theta, \phi)\rangle, |\Psi_{B-\uparrow}(\theta, \phi)\rangle, |\Psi_{A-\downarrow}(\theta, \phi)\rangle, |\Psi_{B-\downarrow}(\theta, \phi)\rangle\}, \quad (\text{S35})$$

310 with the explicit expressions

$$\begin{aligned} |\Psi_{A-\uparrow}(\theta, \phi)\rangle &= \frac{1}{\sqrt{2}} (\cos \theta \cos \phi + i \sin \phi, -\cos \theta \sin \phi + i \cos \phi, 0, \sin \theta, 0, 0, 0, 0)^T, \\ |\Psi_{B-\uparrow}(\theta, \phi)\rangle &= \frac{1}{\sqrt{2}} (i \sin \theta \cos \phi, -i \sin \theta \sin \phi, 1, -i \cos \theta, 0, 0, 0, 0), \\ |\Psi_{A-\downarrow}(\theta, \phi)\rangle &= \frac{1}{\sqrt{2}} (0, 0, 0, 0, \cos \theta \cos \phi + i \sin \phi, -\cos \theta \sin \phi + i \cos \phi, 0, \sin \theta)^T, \\ |\Psi_{B-\downarrow}(\theta, \phi)\rangle &= \frac{1}{\sqrt{2}} (0, 0, 0, 0, i \sin \theta \cos \phi, -i \sin \theta \sin \phi, 1, -i \cos \theta). \end{aligned} \quad (\text{S36})$$

311

312 The second-order perturbed Hamiltonian is given by

$$\Delta \mathcal{H}_P^{eff(2)} = \frac{1}{\Delta E} \left( \langle \Psi_{upper} | (\mathcal{H}_{soc} + \mathcal{H}_{k^2}(\mathbf{k})) \hat{P}_{lower} (\mathcal{H}_{soc} + \mathcal{H}_{k^2}(\mathbf{k})) | \Psi_{upper} \rangle \right), \quad (\text{S37})$$

313 where  $\Delta E = E_+ - E_- = 2A_1 k$  is the energy difference and the projection operator  $\hat{P}_{lower} =$   
 314  $|\Psi_{lower}\rangle \langle \Psi_{lower}|$  onto the lower four bands in Eq. (S35). To simplify the problem, we only consider  
 315 the mixed terms of  $\mathcal{H}_{soc}$  and  $\mathcal{H}_{k^2}(\mathbf{k})$ , given by

$$\Delta\mathcal{H}_P^{eff(2)} = \frac{1}{\Delta E} (\langle \Psi_{upper} | \mathcal{H}_{soc} | \Psi_{lower} \rangle \langle \Psi_{lower} | \mathcal{H}_{k^2}(\mathbf{k}) | \Psi_{upper} \rangle) + \text{h.c.}, \quad (\text{S38})$$

316 The matrix elements of  $\Delta\mathcal{H}_P^{eff(2)}$  are,

$$\left[ \Delta\mathcal{H}_P^{eff(2)} \right]_{1,1} = 2 \sin^2(\theta) \sin(\phi) \cos(\phi) (\sin^3(\theta) \sin(\phi) + \sin(\theta) \cos^2(\theta) \cos(\phi) - \cos^3(\theta)), \quad (\text{S39})$$

$$\left[ \Delta\mathcal{H}_P^{eff(2)} \right]_{1,2} = \sin^2(\theta) \cos(\phi) (\sin^2(\theta) \sin(2\phi) + 2i \cos(\theta) \sin(\phi) (\cos(\theta) (\cos(\theta) \cos(\phi) + \sin(\theta)) + \sin(\phi) (\sin^2(\theta) + i \cos(\theta))))), \quad (\text{S40})$$

$$\left[ \Delta\mathcal{H}_P^{eff(2)} \right]_{1,3} = \frac{1}{4} e^{-i\phi} \sin(\theta) \cos(\theta) (\sin(2\phi) (\sin(3\theta) \sin(\phi) + 4 \cos^3(\theta)) - 8 \sin(\theta) \cos^2(\theta) \sin(\phi) \cos^2(\phi) + 8i \cos(\theta) \sin^2(\phi) + (-\frac{3}{2} + 6i) \sin(\theta) \cos(\phi) + (\frac{3}{2} + 2i) \sin(\theta) \cos(3\phi)), \quad (\text{S41})$$

$$\left[ \Delta\mathcal{H}_P^{eff(2)} \right]_{1,4} = e^{-i\phi} \sin(\theta) ((\cos(\theta) - 1) (\cos^2(\theta) \cos(\phi) + i \sin(\theta) \sin(\phi) \cos(\phi) (-\cos^2(\theta) + \sin(\theta) (\cos(\theta) + i) \cos(\phi)) + \sin(\theta) \cos(\theta) \sin^2(\phi) (-1 - i \sin(\theta) \cos(\phi))) - 2i \cos^2(\frac{\theta}{2}) (-i \cos^2(\theta) \cos(\phi) \cos(2\phi) + \sin(\phi) \cos(\phi) ((\cos^3(\theta) + \cos(\theta)) \cos(\phi) - i \sin^2(\theta) \cos(\phi) + \sin(\theta) \cos^2(\theta)) + \sin(\theta) \cos(\theta) \sin^2(\phi) (\sin(\theta) \cos(\phi) + i))), \quad (\text{S42})$$

and

$$\left[ \Delta\mathcal{H}_P^{eff(2)} \right]_{2,2} = -\frac{1}{4} \sin^5(\theta) \sin(\phi) \sin(2\phi) (\cot^2(\theta) (-4 \cot(\theta) \csc(\phi) + 4 \cot(\phi) - 1) + \csc^2(\theta) + 3), \quad (\text{S43})$$

$$\left[ \Delta\mathcal{H}_P^{eff(2)} \right]_{2,3} = \frac{1}{2} e^{-i\phi} \sin(\theta) \cos(\theta) (-4 \sin(\phi) (\sin(\theta) \sin(\phi) + (2 + 2i) \sin^2(\frac{\theta}{2}) \cos^2(\phi)) + \cos^2(\theta) \sin(2\phi) (-4i \sin^2(\frac{\theta}{2}) \cos(\phi) + 2i \sin(\theta) + \csc(\phi)) + \cos(\theta) \csc(\phi) (- (2 + 2i) \sin^2(\frac{\theta}{2}) \sin^2(2\phi) + \sin^2(\frac{\theta}{2}) \sin(4\phi) + 4i \sin^2(\theta) \sin^3(\phi) \cos(\phi) + \sin(2\phi))), \quad (\text{S44})$$

$$\left[ \Delta\mathcal{H}_P^{eff(2)} \right]_{2,4} = -\frac{1}{8} e^{-i\phi} \sin(\theta) \cos(\theta) (8 \cos^3(\theta) \sin(2\phi) - 16 \sin(\theta) \cos^2(\theta) \sin(\phi) \cos^2(\phi) + 16i \cos(\theta) \sin^2(\phi) + \cos(\phi) (4 \sin(3\theta) \sin^2(\phi) + (-3 + 12i) \sin(\theta)) + (3 + 4i) \sin(\theta) \cos(3\phi)), \quad (\text{S45})$$



and

$$\begin{aligned} \left[ \Delta \mathcal{H}_P^{eff(2)} \right]_{3,3} &= -\frac{1}{4} \sin^5(\theta) \sin(\phi) \sin(2\phi) \\ &\quad (\cot^2(\theta)(-4 \cot(\theta) \csc(\phi) + 4 \cot(\phi) - 1) + \csc^2(\theta) + 3), \end{aligned} \quad (\text{S46})$$

$$\begin{aligned} \left[ \Delta \mathcal{H}_P^{eff(2)} \right]_{3,4} &= -i \sin^2(\theta) \sin(\phi) \cos(\phi) (2 \cos^3(\theta) \cos(\phi) + 2 \cos^2(\theta) (\sin(\theta) + i \sin(\phi))) \\ &\quad + \sin(\theta) (\sin(2\theta) \sin(\phi) - 2i \sin(\theta) \cos(\phi)), \end{aligned} \quad (\text{S47})$$

and

$$\left[ \Delta \mathcal{H}_P^{eff(2)} \right]_{4,4} = 2 \sin^2(\theta) \sin(\phi) \cos(\phi) (\sin^3(\theta) \sin(\phi) + \sin(\theta) \cos^2(\theta) \cos(\phi) - \cos^3(\theta)), \quad (\text{S48})$$

317 And the other parts are related by conjugation  $\left[ \Delta \mathcal{H}_P^{eff(2)} \right]_{i,j} = \left[ \Delta \mathcal{H}_P^{eff(2)} \right]_{j,i}^*$ . The second-order  
 318 perturbation corrections provides the spin-flipping terms in the effective model and thus generates  
 319 a tiny gap for the emergent nodal lines on the Fermi surfaces, as shown in Fig. S22 (c).

320 To simplify the above discussion, we can further project the above four-band  $P$  model to the  
 321 effective model that only consists of the two bands forming the nodal plane. To do that, we  
 322 consider the eigen-states of the model Hamiltonian (S30) and consider two eigen-states  $\{|\alpha =$   
 323  $+, \beta = -\rangle, |\alpha = -, \beta = +\rangle\}$  that give the eigen-energies  $E_{\alpha=+, \beta=-}$  and  $E_{\alpha=-, \beta=+}$  in Eq. S34.  
 324 Within these two eigen-states, the effective Hamiltonian  $\mathcal{H}_P^{eff(1)}$  can be reduced to

$$\mathcal{H}_{eff} = \epsilon_0 + d_z(\mathbf{k}) \sigma_z, \quad (\text{S49})$$

325 where  $\epsilon_0 = C_0 + B_1 k^2 + A_1 k$  and  $d_z(\mathbf{k}) = \lambda_0 - \frac{\sqrt{3}}{4} \tilde{C} k^2 |\sin 2\phi \sin 2\theta \sin \theta| = \lambda_0 - \sqrt{3} \tilde{C} \frac{|k_x k_y k_z|}{k}$ .  
 326 This Hamiltonian is the exactly two-band model discussed in the main text. Due to the SOC with  
 327  $\mathbf{k} \cdot \mathbf{s}$  in the  $P$ -model (S34), the spin texture is hexagonal on each Fermi surfaces ( $\langle \mathbf{s} \rangle \sim \alpha \mathbf{k}$  with  
 328  $\alpha = \pm$ ). Moreover, we plot the spin texture on  $E_{\alpha=+, \beta=-}(k, \theta, \phi) = \epsilon_0 + d_z(\mathbf{k}) = E_f$  in  
 329 Fig. S23 (a), and that for  $E_{\alpha=-, \beta=+}(k, \theta, \phi) = \epsilon_0 - d_z(\mathbf{k}) = E_f$  in Fig. S23 (b). It indicates  
 330 that the crossings between these two Fermi surfaces have opposite spin-polarization. Therefore,  
 331 according to the low-energy effective Hamiltonian, we can conclude that the spin-conservation  
 332 plays the role of the quasi-symmetry.

333 Now we discuss the breaking of the quasi-symmetry by second-order perturbation corrections.  
 334 To see that, we can further project  $\mathcal{H}_P^{eff(2)}$  into the subspace of  $\{|\alpha = +, \beta = -\rangle, |\alpha = -, \beta =$   
 335  $+\rangle\}$  and the effective Hamiltonian will include two more terms as

$$\mathcal{H}_{eff(2)} = \delta d_x(\mathbf{k})\sigma_x + \delta d_y(\mathbf{k})\sigma_y, \quad (\text{S50})$$

336 which are due to the spin-flipping terms, breaking the quasi-symmetry. As a result, the co-  
 337 dimension of the nodal plane becomes 3 instead of 1, explaining the gap opening. While the  
 338 detailed expressions for  $\delta d_x$  and  $\delta d_y$  are complex, we give an estimate of the typical magnitude  
 339 of the gap  $\Delta_{eff(2)} = 2\sqrt{(\delta d_x)^2 + (\delta d_y)^2} \sim 0.8 \text{ meV}$  for  $k_F = 0.13 \text{ \AA}^{-1}$ , being the same order  
 340 with the DFT estimations [see FIG. S11]. By solving  $d_z(\mathbf{k}) = 0$  in Eq. (S49), we can find the  
 341 nodal line on the  $\Gamma - R - M$  plane ( $\phi = \pi/4$ ) that is shown in Fig. S23 (c). Furthermore, we  
 342 calculate the energy gap ( $\sqrt{(\delta d_x(\mathbf{k}))^2 + (\delta d_y(\mathbf{k}))^2}$ ) for the nodal line on the  $\Gamma - R - M$  plane,  
 343 shown in Fig. S23 (d). Please note that the gap vanishes for the type-II Weyl point which locates  
 344 at  $\theta = \arcsin(\sqrt{2/3}) \sim 0.96$  (along the  $\Gamma - R$  line), due to the  $C_3$  protection (the two Weyl states  
 345 have different  $C_3$ -eigenvalues).

#### 346 **D. The Berry curvature distributions**

347 In this section, we show the topologically physical consequence for the emergent nodal lines  
 348 (near crossing), characterized by the Berry curvature distributions in the momentum space. We  
 349 calculate the Berry curvature based on the  $R$ -model in the  $\Gamma - R - M$  plane. Here, we take a  
 350 standard formula to compute the gauge-invariant Berry curvature

$$\Omega_n(\mathbf{k}) = -\text{Im} \sum_{m \neq n} \frac{\langle n | \nabla \mathcal{H}_R(\mathbf{k}) | m \rangle \times \langle m | \nabla \mathcal{H}_R(\mathbf{k}) | n \rangle}{(E_m - E_n)^2}, \quad (\text{S51})$$

351 where the velocity operators are given by  $\hat{\mathbf{V}} = \nabla \mathcal{H}_R(\mathbf{k}) \triangleq (\hat{V}_x, \hat{V}_y, \hat{V}_z)$ . Similar to the analysis  
 352 in Re. [6] (see Eq. (37) in the Supplementary Materials for the Nature paper of MnSi), we find that

$$S_{2x}\mathcal{T} : (k_x, k_y, k_z) \rightarrow (-k_x, k_y, k_z) \text{ and } \mathbf{\Omega}(k_x, k_y, k_z) = \mathbf{\Omega}(-k_x, k_y, k_z) \begin{pmatrix} -1 & 0 & 0 \\ 0 & +1 & 0 \\ 0 & 0 & +1 \end{pmatrix}, \quad (\text{S52})$$

$$S_{2y}\mathcal{T} : (k_x, k_y, k_z) \rightarrow (k_x, -k_y, k_z) \text{ and } \mathbf{\Omega}(k_x, k_y, k_z) = \mathbf{\Omega}(k_x, -k_y, k_z) \begin{pmatrix} +1 & 0 & 0 \\ 0 & -1 & 0 \\ 0 & 0 & +1 \end{pmatrix}, \quad (\text{S53})$$

$$S_{2z}\mathcal{T} : (k_x, k_y, k_z) \rightarrow (k_x, k_y, -k_z) \text{ and } \mathbf{\Omega}(k_x, k_y, k_z) = \mathbf{\Omega}(k_x, k_y, -k_z) \begin{pmatrix} +1 & 0 & 0 \\ 0 & +1 & 0 \\ 0 & 0 & -1 \end{pmatrix}, \quad (\text{S54})$$

353 where we take the vector for Berry curvature as  $\mathbf{\Omega}_n(k_x, k_y, k_z) = (\Omega_{n,yz}, \Omega_{n,zx}, \Omega_{n,xy})$  for the  
354  $n$ -th band. The calculated results are shown in Fig. S24 on the  $\Gamma - R - M$  plane, confirming the  
355 above symmetry requirements. Here we present the Berry curvature for the  $1^-$ -band (see the band  
356 notation in Fig. 2 (d) in the main text). Namely, this band is just the second upper-band from the  
357  $\mathbf{k} \cdot \mathbf{p}$ -bands, shown in Fig. S21 (c). The three components are shown in Fig. S24 (a),(b) and (c),  
358 where the four Fermi surfaces are shown with  $E_f = -0.06$  eV. Moreover, the Berry curvature  
359 distribution coincides with the emergent nodal lines, illustrated in Fig. S24 (d),(e) and (f). At the  
360  $R$ -point or Weyl points, the  $U(1)$  Berry curvature is not well defined due to degeneracy, which  
361 corresponds to the singularity. In Fig. S24 (a), (b) and (c), the singularity at the  $R$ -points is due to  
362 the 6-fold degeneracy. And the type-II Weyl points are shown in Fig. S24 (d) for the singularity  
363 (marked by the dark-red solid circle).

### 364 E. The strain effects on the crystalline symmetries and quasi-symmetries

In this subsection, we study the strain effect on the electronic bands, which is characterized by the strain tensor

$$u_{ij} = \frac{1}{2} (\partial_{x_i} u_j + \partial_{x_j} u_i) \quad (\text{S55})$$

where  $u_i$  is the displacement at  $\mathbf{x}$ . And  $u_{ij}$  transfers as  $k_i k_j$  under point group symmetry operators. Thus, the leading order correction to the 8-band R-model in Eq. (S19) due to the strain-induced Hamiltonian is generally given by

$$\begin{aligned} \mathcal{H}_{strain} = & D_0(u_{xx} + u_{yy} + u_{zz}) + D_1(u_{xy}\sigma_z\tau_0 + u_{yz}\sigma_0\tau_z + u_{xz}\sigma_z\tau_z) \\ & + D_2(u_{xy}\sigma_x\tau_x - u_{yz}\sigma_0\tau_x + u_{xz}\sigma_x\tau_0) + D_3(u_{xy}\sigma_x\tau_z - u_{yz}\sigma_y\tau_y - u_{xz}\sigma_z\tau_x). \end{aligned} \quad (\text{S56})$$

365 It is invariant under both all the symmetry generators of the space group 198 and the time-reversal  
366 symmetry operator  $\mathcal{T} = i s_y \mathcal{K}$  with  $\mathcal{K}$  the complex conjugate.

Here, we first describe the calculation of the strain tensor resulting from an uniaxial stress of magnitude  $P$  along an arbitrary direction. Analysis begins by adopting a coordinate system  $(x', y', z')$  in which the  $x'$  axis is parallel to the stress direction. This system is related to the coordinate system  $(x, y, z)$  of the primary crystallographic axes of the semiconductor by a rotation

$$U(\theta, \phi) = \begin{pmatrix} \cos(\theta) \cos(\phi) & \cos(\theta) \sin(\phi) & -\sin(\theta) \\ -\sin(\phi) & \cos(\phi) & 0 \\ \sin(\theta) \cos(\phi) & \sin(\theta) \sin(\phi) & \cos(\theta) \end{pmatrix} \quad (\text{S57})$$

where  $\theta$  and  $\phi$  are the polar and azimuthal angles of the stress direction relative to the crystallographic coordinate system. In the primed coordinate system, the stress tensor has only one non-zero component,  $\sigma'_{zz} = P$ . The stress tensor in the crystallographic system can be calculated from

$$\sigma_{ij} = U_{\alpha i} U_{\beta j} \sigma'_{\alpha\beta}. \quad (\text{S58})$$

If uniaxial stress is applied along one of the directions [100], [110], and [111], the related stress tensors in the principal system become:

$$\sigma_{[100]} = \begin{pmatrix} P & 0 & 0 \\ 0 & 0 & 0 \\ 0 & 0 & 0 \end{pmatrix}, \sigma_{[110]} = \begin{pmatrix} P/2 & P/2 & 0 \\ P/2 & P/2 & 0 \\ 0 & 0 & 0 \end{pmatrix}, \sigma_{[111]} = \begin{pmatrix} P/3 & P/3 & P/3 \\ P/3 & P/3 & P/3 \\ P/3 & P/3 & P/3 \end{pmatrix}, \quad (\text{S59})$$

Then, we study with the (110) strain, whose lowest order strain Hamiltonian reads,

$$\mathcal{H}_{(110)strain} = D_0(u_{xx} + u_{yy}) + D_1(u_{xy}\sigma_z\tau_0) + D_2(u_{xy}\sigma_x\tau_x) + D_3(u_{xy}\sigma_x\tau_z). \quad (\text{S60})$$

In the following, the  $u_{xx}$  and  $u_{yy}$  are absorbed into the Fermi energy, thus only  $u_{xy}$ -terms will be considered. Let us check the symmetry breaking, the  $S_{2x} = i\sigma_y\tau_0$  and  $S_{2y} = i\sigma_x\tau_y$  are broken,

while the  $S_{2z} = i\sigma_z\tau_y$  is still preserved because of

$$[S_{2z}, \mathcal{H}_{(110)strain}] = 0. \quad (\text{S61})$$

367 It indicates that the strain-induced gaps only appear for two high-symmetry planes:  $k_x = 0$  or  
 368  $k_y = 0$ ; while the  $k_z = 0$  plane still has twofold degeneracy. Moreover, let us also check the  $R$ -  
 369 point with  $k_x = k_y = k_z = 0$ , only  $\mathcal{T}$  and  $S_{2z}$  are preserved, all the other symmetries are broken,  
 370 then, each state is twofold degenerate.

To confirm the above symmetry analysis, we plot the bands without/with strain effect in Fig. S26, where we use the strain parameters:  $D_1 = 0.003$ ,  $D_2 = 0.001$ , and  $D_3 = 0.002$  in unit of eV. From Fig. S26 (a) and (b), we can see the bands along  $k_z = 0$  line are still degenerate. However, in (c) and (d), the bands along  $k_x, k_y = 0$  are no longer degenerate due to strain effect (crystalline symmetry breaking). In (e), the Weyl point is no longer along the  $\Gamma - R$  line since the  $C_3$  rotation is broken. Based on the bands in the  $\Gamma - R - M$  plane, we define two gaps as

$$\Delta_{cs} = |E_{1+}(0, 0, 0.2) - E_{1-}(0, 0, 0.2)|, \quad (\text{S62})$$

$$\Delta_{qs} = \min |E_{1-}(k, k, k_z) - E_{2+}(k, k, k_z)|. \quad (\text{S63})$$

371 where the crystalline-symmetry gap  $\Delta_{cs}$  represents the breaking of  $S_{2x}$  and the quasi-symmetry  
 372 gap  $\Delta_{qs}$  is for the quasi-symmetry gap (near degeneracy). As shown in (f), we conclude that the  
 373 quasi-symmetry is almost unaffected by the strain.

Next, we further consider the the (11 $\delta$ ) and (111) strain effects, whose Hamiltonian can be represented as

$$\mathcal{H}_{(11\delta)strain} = D_1(u_{xy}\sigma_z\tau_0) + D_2(u_{xy}\sigma_x\tau_x) + D_3(u_{xy}\sigma_x\tau_z) + D_4(u_{xy}\sigma_0\tau_z), \quad (\text{S64})$$

$$\mathcal{H}_{(111)strain} = D_1(u_{xy}\sigma_z\tau_0 + u_{yz}\sigma_0\tau_z + u_{xz}\sigma_z\tau_z). \quad (\text{S65})$$

374 The additional terms due to (11 $\delta$ ) strain might be in principle smaller than those parameters used  
 375 for (110) strain. Notice that the Hamiltonian for (11 $\delta$ ) strain has been simplified, so only a  $D_4$   
 376 term is added, compared with the Hamiltonian of (110) strain. To illustrate clearly the breaking of  
 377  $S_{2z}$  rotation by  $D_4$  term, we take  $D_4$  as the same order as  $D_1$ .

378 To schematically demonstrate these strain effects on the electronic Fermi surfaces, we plot the  
 379 Fermi surfaces perpendicular to (100), ( $\bar{1}\bar{1}0$ ) and (111) axes in Fig. S27. As expected, once the  
 380 crystalline symmetry is easily broken by the strain, the crystalline symmetry-protected twofold  
 381 degeneracy is spitted. Thus, we may conclude that, the breaking of crystalline symmetry due

382 to strain effect, more magnetic orbits can be observed due to trivial magnetic breakdown. It is  
 383 consistent with the experimental observations of quantum oscillation measurement.

By using perturbation theory discussed in Sec. **VIII C**, we discuss the strain effect on the robustness of the quasi-symmetry in CoSi. To the first-order perturbation, we find the  $P$ -model around  $R$ -point that is modified as,

$$\mathcal{H}_P = \mathcal{H}_{\text{soc},+}^{\text{eff}(1)} + \mathcal{H}_{k^2,+}^{\text{eff}(1)} + \mathcal{H}_{\text{strain}}, \quad (\text{S66})$$

where each part reads

$$\begin{aligned} \mathcal{H}_{\text{soc},+}^{\text{eff}(1)} &= \lambda_0 (\lambda_x s_x + \lambda_y s_y + \lambda_z s_z) \omega_0, \\ \mathcal{H}_{k^2,+}^{\text{eff}(1)} &= s_0 (d_x \omega_x + d_y \omega_y + d_z \omega_z), \\ \mathcal{H}_{\text{strain}} &= s_0 (d'_x \omega_x + d'_y \omega_y + d'_z \omega_z), \end{aligned} \quad (\text{S67})$$

where the coefficients are defined as

$$\begin{aligned} (\lambda_x, \lambda_y, \lambda_z) &= (\sin \theta \cos \phi, \sin \theta \sin \phi, \cos \theta) = \frac{\mathbf{k}}{|\mathbf{k}|}, \\ d_x &= \frac{\tilde{C}k^2}{4} \sin \theta \sin(2\theta) \sin(2\phi) (\cos \phi + \sin \phi), \\ d_y &= \frac{\tilde{C}k^2}{4} \sin \theta \sin(2\theta) \sin(2\phi) (\sin \theta + \cos \theta (\cos \phi - \sin \phi)), \\ d_z &= \frac{\tilde{C}k^2}{4} \sin \theta \sin(2\theta) \sin(2\phi) (\cos \theta - \sin \theta (\cos \phi - \sin \phi)), \\ d'_x &= u_{xy} \cos(\theta) (-d_2 \sin(\phi) + d_3 \cos(\phi)), \\ d'_y &= u_{xy} \cos(\theta) (-d_2 \cos(\theta) \cos(\phi) - d_3 \cos(\theta) \sin(\phi) - d_1 \sin(\theta)), \\ d'_z &= u_{xy} \cos(\theta) (\sin(\theta) (d_3 \sin(\phi) + d_2 \cos(\phi)) + d_1 \cos(\theta)). \end{aligned} \quad (\text{S68})$$

As a result, we find that the new  $P$ -model in Eq. (S66) with corrections from the strain effect is still a stabilizer code Hamiltonian, the quasi-symmetry  $\mathcal{M}_{\text{eff}}$  is still preserved. Thus, the dispersion consists two parts,

$$E_{\alpha,\beta} = \alpha \lambda_0 + \beta \sqrt{(d_x + d'_x)^2 + (d_y + d'_y)^2 + (d_z + d'_z)^2}, \quad (\text{S69})$$

where the second part is give by

$$\frac{1}{2} \sqrt{3\tilde{C}^2 k_r^4 \sin^4(\theta) \cos^2(\theta) \sin^2(2\phi) + \tilde{C} \tilde{d} u_{xy} k_r^2 \sin^2(2\theta) \sin(2\phi) + 4(d_1^2 + d_2^2 + d_3^2) \cos^2(\theta) u_{xy}^2}, \quad (\text{S70})$$

here  $\tilde{C} = C_1 - C_2 + C_3$  and  $\tilde{d} = d_1 - d_2 + d_3$ . Please note that

$$\sin^2(\theta) \cos(\theta) \sin(2\phi) \times \cos(\theta) = \frac{1}{4} \sin^2(2\theta) \sin(2\phi), \quad (\text{S71})$$

therefore, Eq. (S70) becomes

$$\frac{1}{2} \sqrt{\left(\tilde{C}\tilde{k} + d_1 u_{xy} \cos(\theta)\right)^2 + \left(\tilde{C}\tilde{k} + d_3 u_{xy} \cos(\theta)\right)^2 + \left(\tilde{C}\tilde{k} - d_2 u_{xy} \cos(\theta)\right)^2} \quad (\text{S72})$$

where we have defined  $\tilde{k} = k_r^2 \sin^2(\theta) \cos(\theta) \sin(2\phi) = 2k_x k_y k_z / k_r$ . The constraint equation for the nodal plane is

$$\lambda_0 = \frac{1}{2} \sqrt{\left(\tilde{C}\tilde{k} + d_1 u_{xy} \cos(\theta)\right)^2 + \left(\tilde{C}\tilde{k} + d_3 u_{xy} \cos(\theta)\right)^2 + \left(\tilde{C}\tilde{k} - d_2 u_{xy} \cos(\theta)\right)^2}. \quad (\text{S73})$$

384 The general solution is plotted in Fig. S28. Recall that, in the  $d_1 = d_2 = d_3 = 0$  limit (no strain),  
385 the above equation is  $\lambda_0 = \sqrt{3}\tilde{C}|k_x k_y k_z|/k_r$ , which is reduced back to our previous results.

Next, let us consider a simple case with by setting  $d_2 = d_3 = 0$ , the equation becomes

$$\lambda_0 = \frac{1}{2} \sqrt{\left(\tilde{C}\tilde{k} + d_1 \cos(\theta)\right)^2 + 2\left(\tilde{C}\tilde{k}\right)^2} = \frac{\tilde{C}}{2} \left| \frac{k_z}{k_r} \right| \times \sqrt{(2k_x k_y + d_1)^2 + 8k_x^2 k_y^2} \quad (\text{S74})$$

386 where  $u_{xy} = 1$  is used for simplicity. In principle, it could also leads to the nodal plane solution,  
387 which indicates that the quasi-symmetry protected nodal plane are robust against strain effect. And  
388 Eq. (S74) gives rise to the following results,

- 389 1.)  $k_z = 0$ , each band has two-fold degeneracy. Thus, there are only two Fermi surfaces. Since  
390  $C_{2z}$  is still preserved for the (110) strain.
- 2.)  $k_x = 0$  or  $k_y = 0$ , the crystalline symmetry protected twofold degeneracy is broken, and the  
gap is about

$$\Delta = \sqrt{d_1^2 + d_2^2 + d_3^2 u_{xy}} |\cos \theta| \quad (\text{S75})$$

- 3.) If Eq. (S74) has physical solutions, it means there is quasi-symmetry protected nodal plane.  
First, let us analytically understand Eq. (S74). By fixing  $k_z \neq 0$ , we get the equation in the  
 $k_x - k_y$  plane,

$$(2k_x k_y + d_1)^2 + 8k_x^2 k_y^2 = (f_\lambda(k_x, k_y, k_z))^2 \quad (\text{S76})$$

391 where  $f_\lambda(k_x, k_y, k_z) = \frac{2\lambda_0}{C} \left| \frac{k_r}{k_z} \right| > 0$ . For  $d_1 = 0$ , nodal plane locates at  $k_x k_y \neq 0$ . When  
392  $d_1 > 0$ , and it is increased, at the critical value  $\frac{2\lambda_0}{C}$ , two nodal planes with  $k_x k_y > 0$  touch  
393 with each other at  $k_x = k_y = 0$ , forming a single nodal plane. We further increase  $d_1$ , then,  
394 the location of nodal planes depends on the value of  $k_z$ .

395 As a brief conclusion, the quasi-symmetry is a symmetry of the lowest Hamiltonian, but not  
396 symmetry of the crystal. It explains that the strain effect does not affect the quasi-symmetry, which  
397 is consistent with the experiments.

- 
- 398 <sup>1</sup> Koepernik, K., and Eschrig, H. Full-potential nonorthogonal local-orbital minimum-basis band-structure  
399 scheme. *Phys. Rev. B* **59**, 1743 (1999).
- 400 <sup>2</sup> Perdew, J. P., Burke, K., and Ernzerhof, M. Generalized gradient approximation made simple. *Phys.*  
401 *Rev. Lett.* **77**, 3865 (1996).
- 402 <sup>3</sup> Blount, E. I. Bloch Electrons in a Magnetic Field. *Phys. Rev.* **126**, 1636 (1962).
- 403 <sup>4</sup> Fortin, J., Bellissard, J., Gusmao, M., and Ziman, T. de Haas–van Alphen oscillations and magnetic  
404 breakdown: Semiclassical calculation of multiband orbits. *Phys. Rev. B* **57**, 1484 (1998).
- 405 <sup>5</sup> Bradlyn, B., Cano, J., Wang, Z., Vergniory, M. G., Felser, C., Cava, R. J., and Bernevig, B. A. Beyond  
406 Dirac and Weyl fermions: Unconventional quasiparticles in conventional crystals. *Science* **353**, aaf5037  
407 (2016).
- 408 <sup>6</sup> Wilde, M. A., Dodenhöft, M., Niedermayr, A., Bauer, A., Hirschmann, M. M., and Alpin, K. et al.,  
409 Symmetry-enforced topological nodal planes at the Fermi surface of a chiral magnet. *Nature* **594**,  
410 374–379 (2021).
- 411 <sup>7</sup> Xu, X., Wang, X., Cochran, T. A., Sanchez, D. S., Chang, G., and Belopolski, I. et al., Crystal growth  
412 and quantum oscillations in the topological chiral semimetal CoSi. *Phys. Rev. B* **100**, 045104 (2019).
- 413 <sup>8</sup> Huber, N., Alpin, K., Causer, G. L., Worch, L., Bauer, A., Benka, G. et al., Network of topological nodal  
414 planes, multifold degeneracies, and Weyl points in CoSi. *arXiv:2107.02820* (2021).



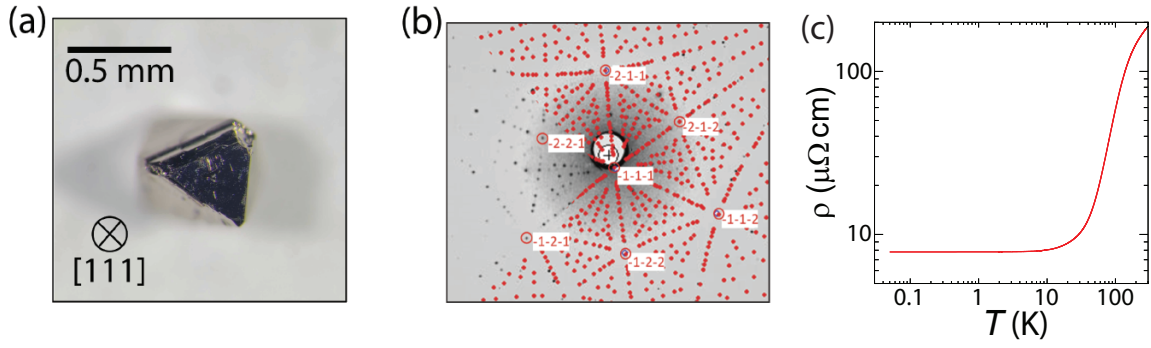


FIG. S1. (a) Optical microscope image of a CoSi single crystal sample. (b) Laue diffraction pattern of the grown CoSi single crystal, superimposed with a theoretically simulated one confirming high crystalline quality. (c) Temperature dependence of resistivity of device-1 measured with electrical current applied along [100] direction.

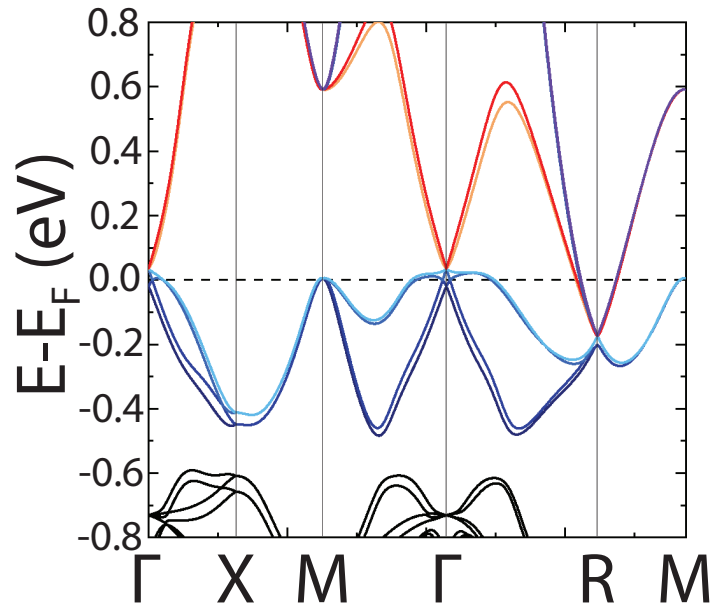


FIG. S2. Ab-initio-calculated band structure of CoSi.

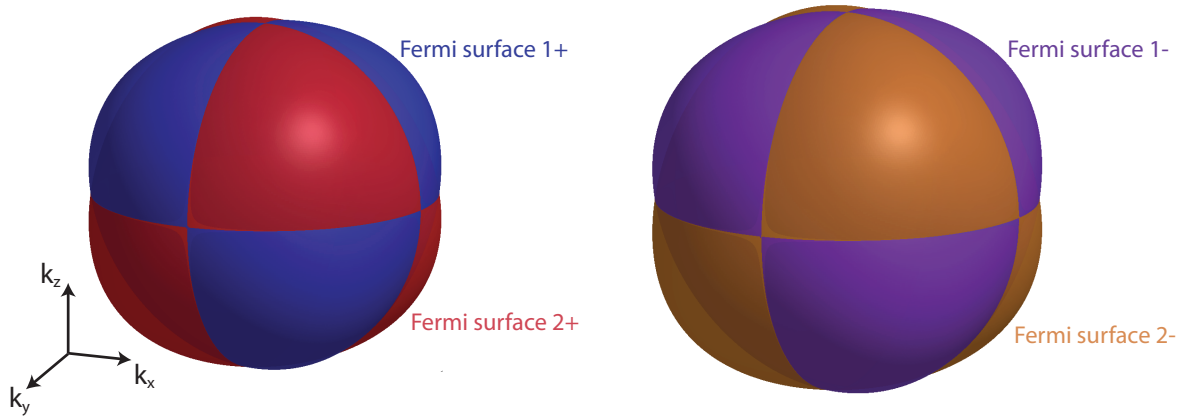


FIG. S3. Fermi surface identification. Two pairs of Fermi surfaces are presented and labelled with their band characters, consistent with the identification in band structure calculations.

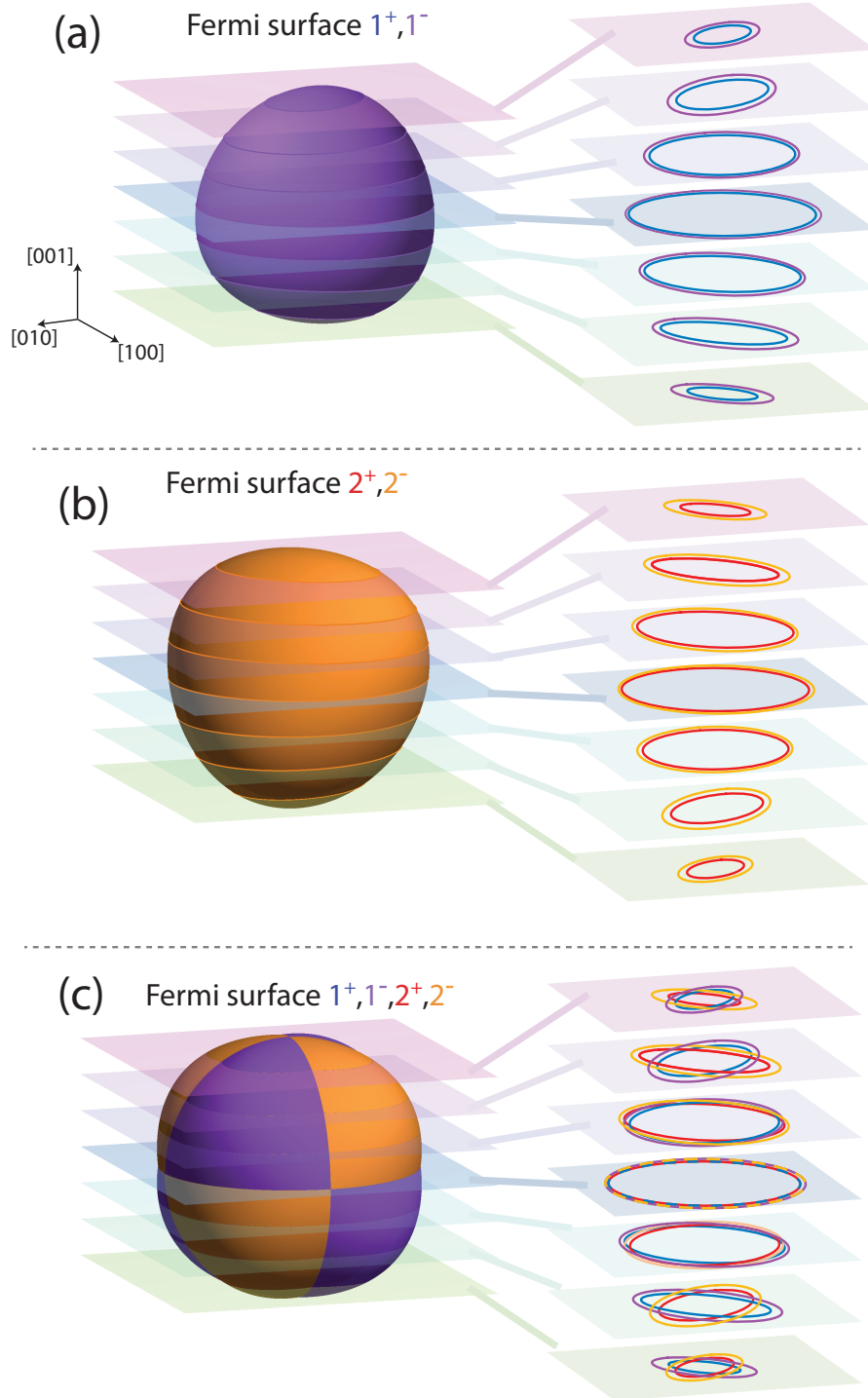


FIG. S4. (a) and (b) present the slice-and-view of Fermi surfaces  $1^\pm$  and  $2^\pm$  respectively. As one can clearly see the sliced orbits of  $1^-$  or  $2^-$  are always larger than  $1^+$  or  $2^+$  at any level. This difference is due to spin splitting caused by spin-orbital coupling (SOC). (c) The summarized view of all four Fermi surfaces. It displays four orbits intersect with each other in a complex pattern which results in the degenerate points protected by either crystalline symmetry or quasi-symmetry.

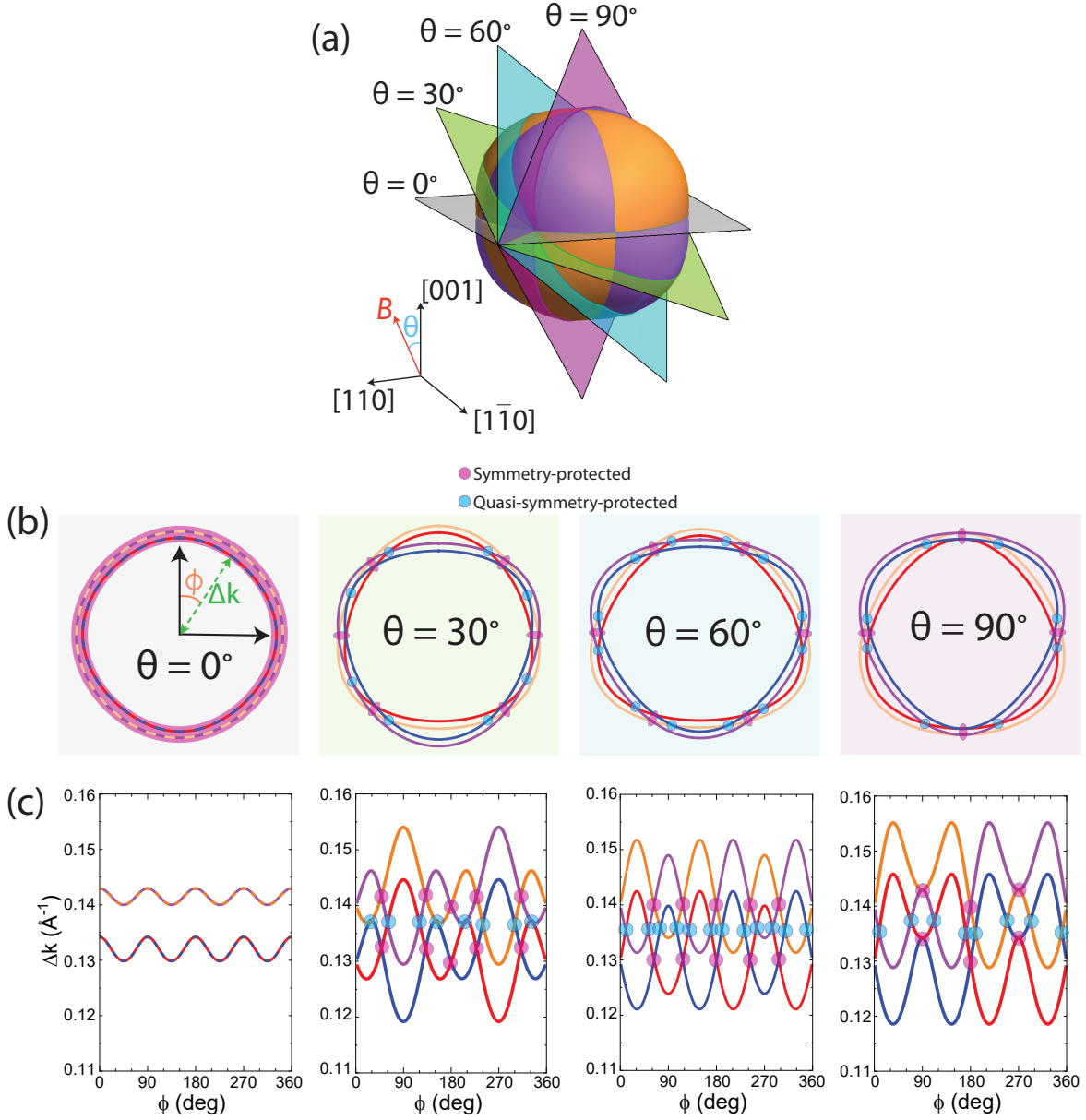


FIG. S5. (a) Illustration of the rotation of magnetic field and the corresponding extremal cross section of Fermi surfaces. Here  $\theta$  is defined as the angle between field direction and  $[001]$  direction, while the square planes stand for the planes perpendicular to the magnetic field. (b) Angle-dependent Fermi surface orbits. The crystalline symmetry and quasi-symmetry protected degeneracies are denoted with pink and blue circles respectively. (c) Momentum difference from R-point  $\Delta k$  as a function of  $\phi$ , which is defined in (b), different types of degenerate points are colored following the color-code in (b).

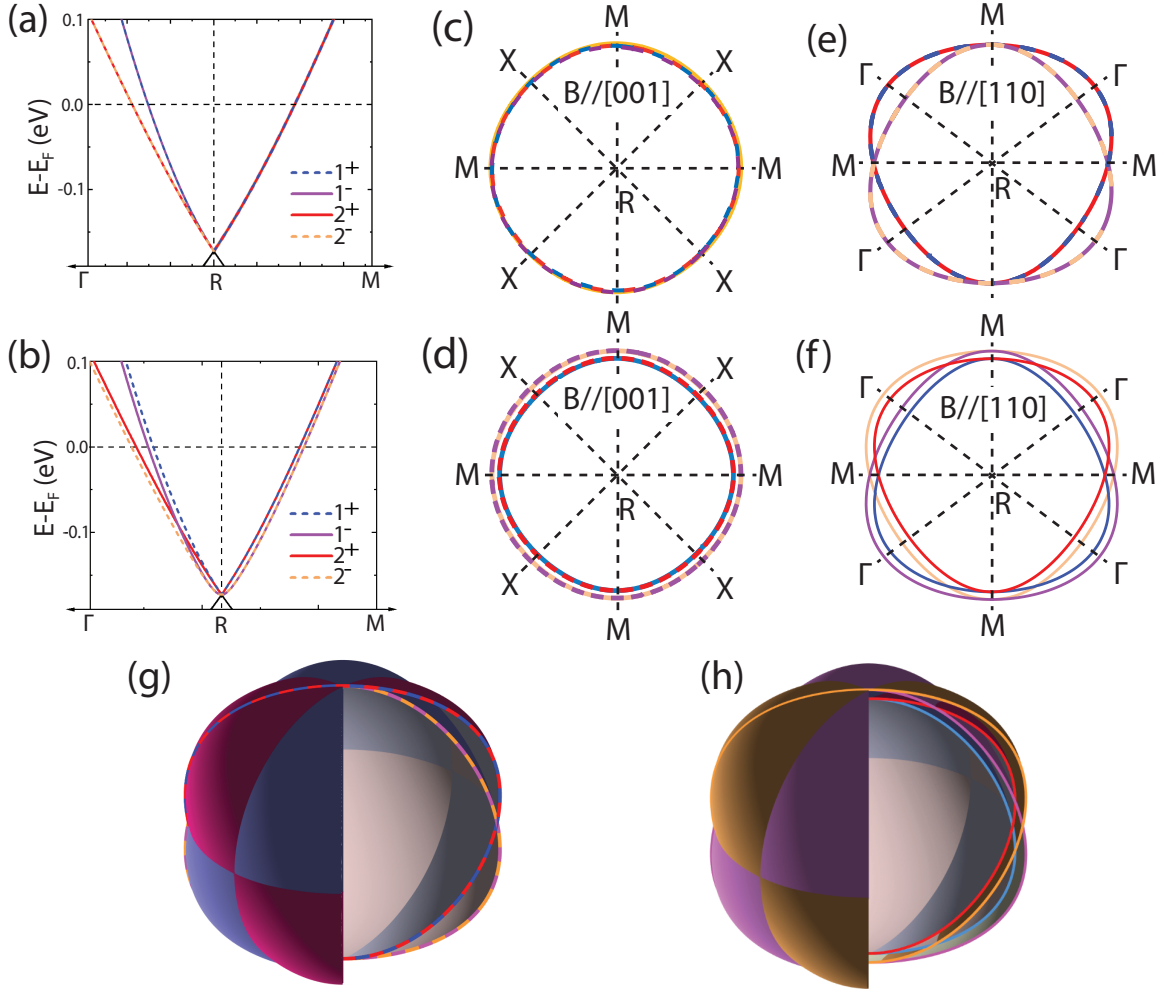
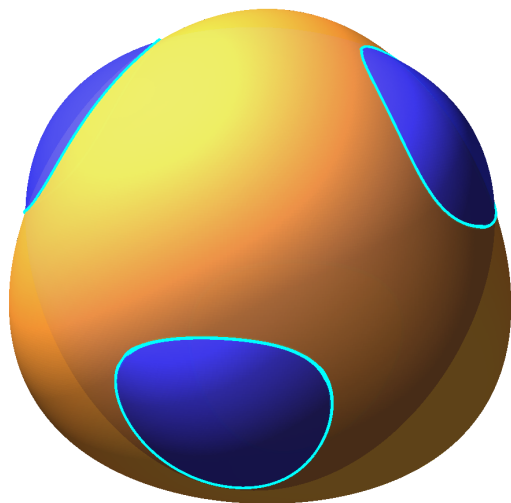


FIG. S6. (a) and (b) display the results of ab-initio band structure calculation around R-point without and with SOC respectively. When SOC is neglected, spin degeneracy is preserved and therefore all bands are at least two-fold degenerate. At the Brillouin zone boundary (i. e. R to M) all four bands are degenerate due to the protection of crystalline symmetry. Taking SOC into account, the spin degeneracy is therefore lifted and only at the Brillouin zone boundary the bands are fully two fold degenerate due to orbital degree of freedom. This spin splitting effect is also clearly demonstrated with the Fermi surface orbit presented in (c) to (f). At the high symmetry (100) plane, the orbits sit exactly at the zone boundary and therefore for (c) non-SOC case all four orbits are degenerate while for (d) SOC-included case they are doubly degenerate. Meanwhile for orbits sit at the (110) plane, the non-SOC scenario features two spin-degenerate orbits that show four-fold degeneracy only at the zone boundary. While for SOC-included case, the four non-degenerate orbits display a intersecting pattern which results in not only the similar degeneracy protected by crystalline symmetry but also quasi-symmetry protected degeneracies that are not located at the high symmetry directions.

Fermi surface  $1^+, 2^-$



Fermi surface  $1^-, 2^+$

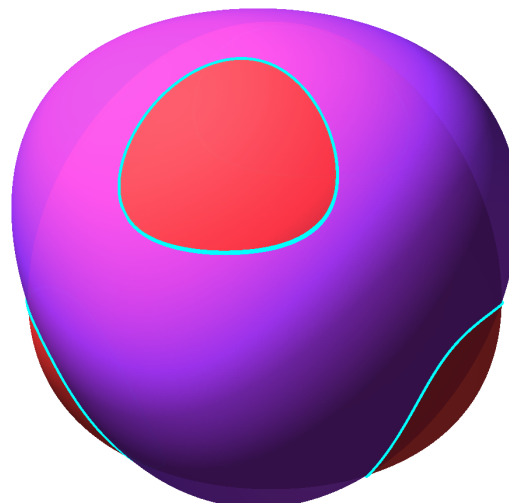


FIG. S7. To clearly demonstrate the intersecting pattern of the Fermi surfaces, here we plot the Fermi surfaces  $1^+/2^-$  and  $1^-/2^+$ , they intersect at the quasi-symmetry protected degenerate rings.

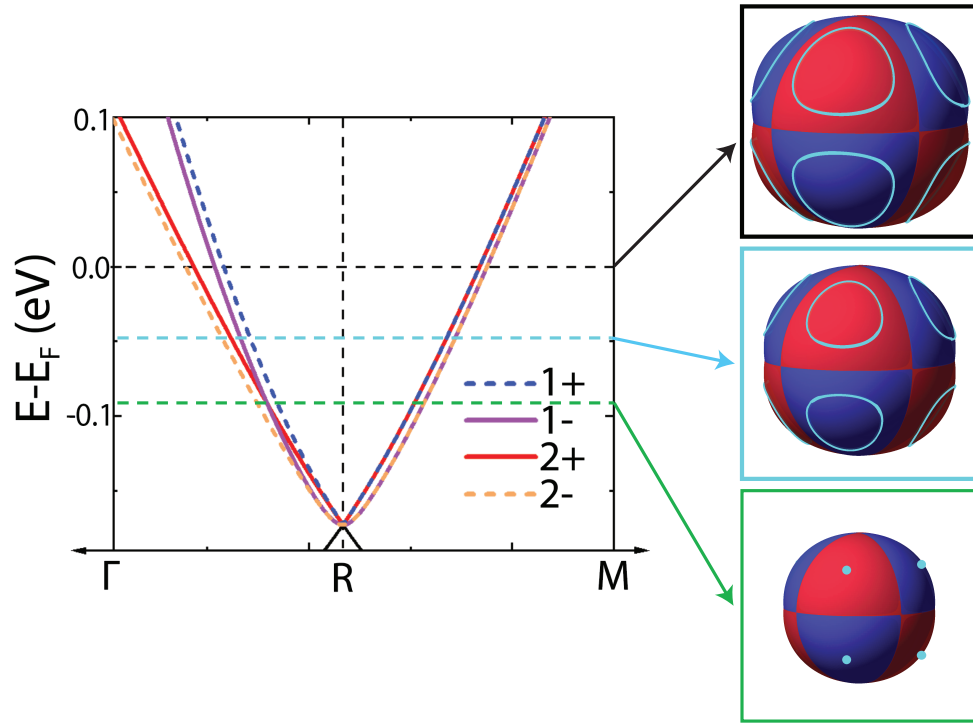


FIG. S8. Fermi energy-dependence of Fermi surfaces  $1^+$  and  $2^+$ . Except for the natural reduction of Fermi surface size, the degenerate rings also become smaller with lower Fermi energy. And when the Fermi level locates exactly at the type-II Weyl node, the rings shrink and reshape to eight Weyl points.

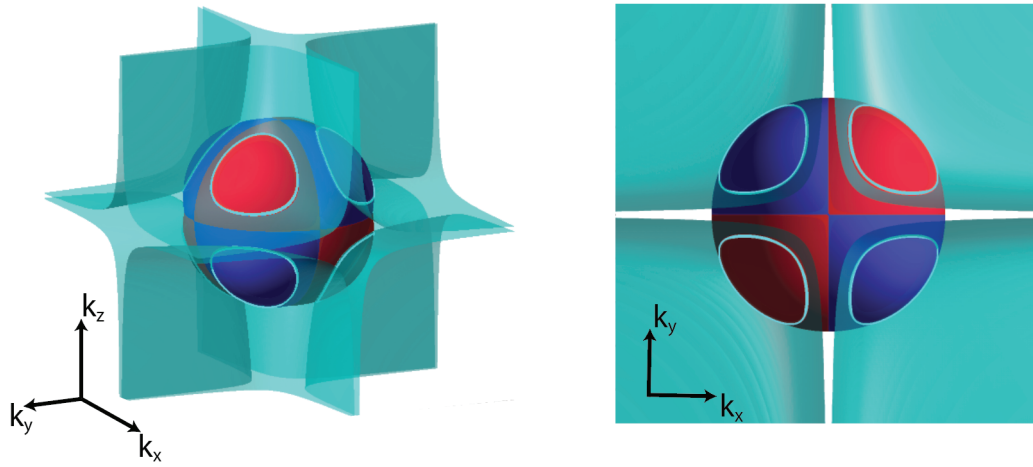


FIG. S9. Fermi surfaces  $1^{+}/2^{+}$  and quasi-symmetry protected degenerate planes. They intersect exactly at the eight degenerate rings.

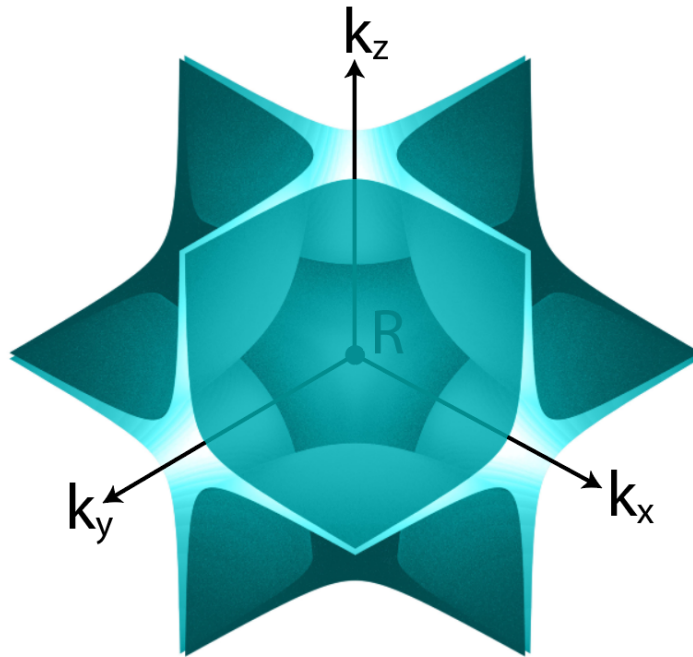


FIG. S10. The eight quasi-symmetry protected degenerate planes.



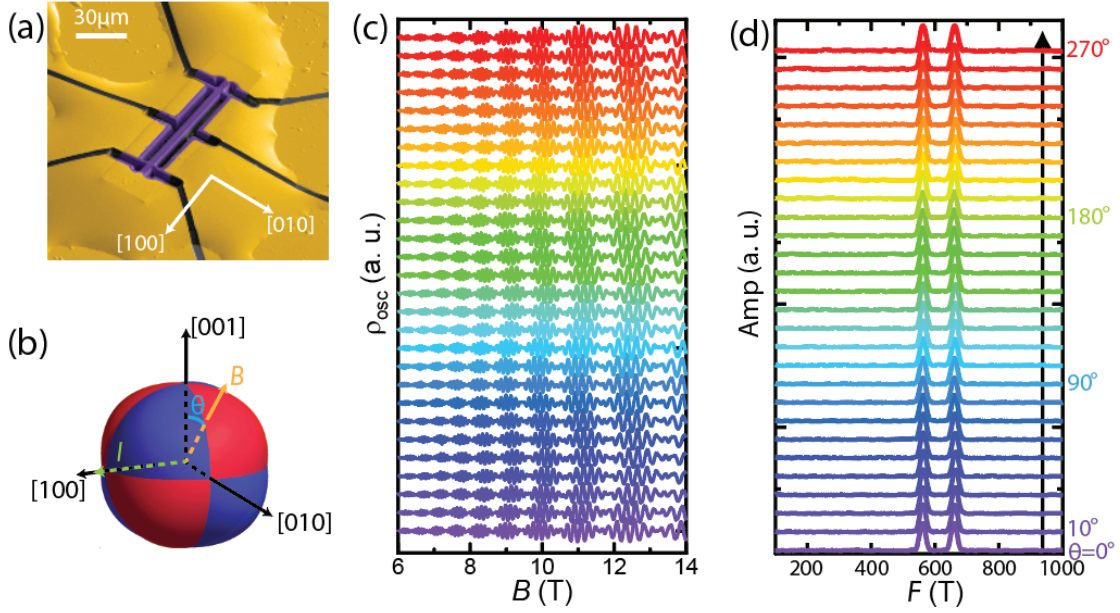


FIG. S11. (a) Scanning electron microscope (SEM) image of device-1. A long bar of a 6 by 6  $\mu\text{m}^2$  cross section is fabricated with FIB. The golden part stands for the deposited gold thin film for obtaining low resistance ohmic contact and the CoSi crystalline part is colored purple. (b) Illustration of field and current orientation of Shubnikov-de-Hass oscillation measurements.  $\theta$  is defined as the angle between the applied field and [001] axis. (c) SdH oscillations as a function of angle  $\theta$ . Here  $\rho_{osc} = \Delta\rho/\rho_{BG}$  with  $\Delta\rho$  the oscillating part of the magnetoresistance (MR) and  $\rho_{BG}$  the MR background subtracted by a 3<sup>rd</sup>-order polynomial function. (d) Fast-Fourier-transformation spectrum of SdH oscillations displayed in (c). The two main peaks correspond to two pairs of Fermi surface orbits with same cross section areas.

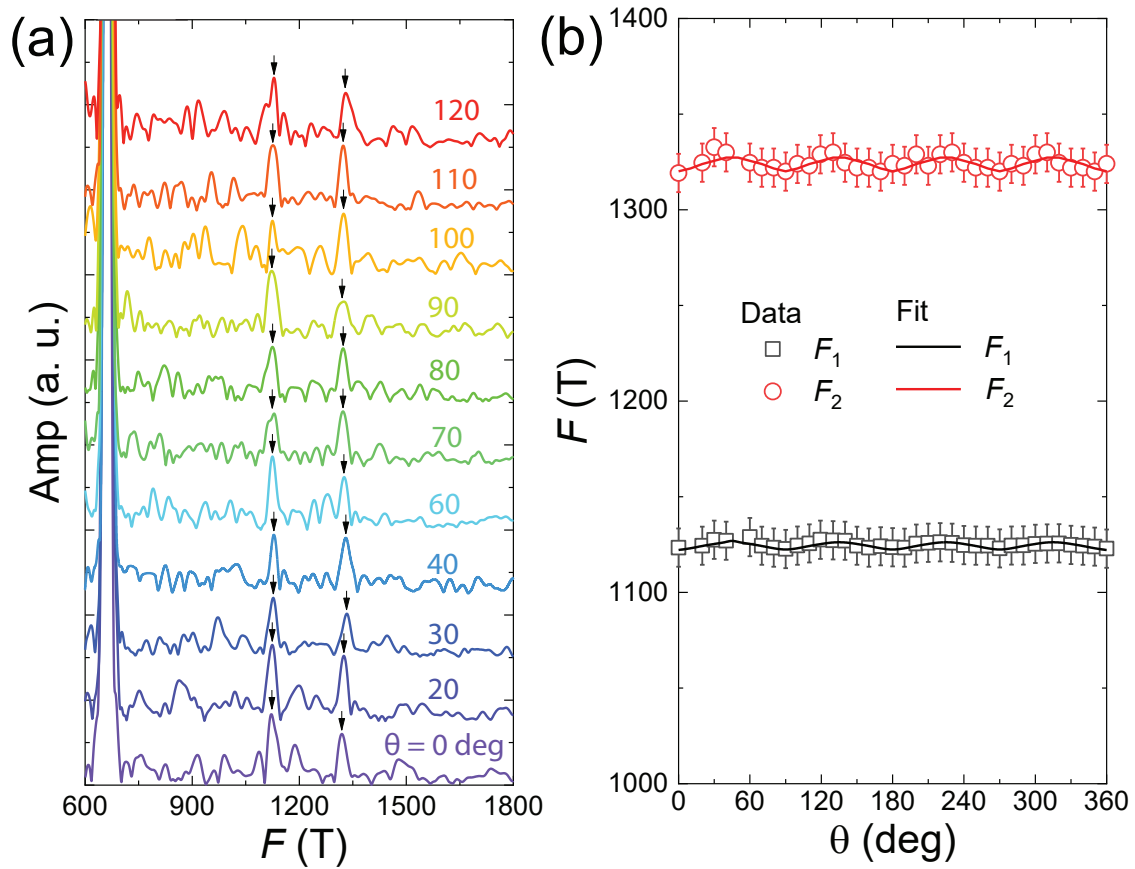


FIG. S12. Analysis of angle-dependent frequencies corresponding to the second harmonic oscillations. Despite of the larger error bar, the angular dependence of the extracted frequencies can still be nicely described by the quasi-symmetry-protected breakdown orbit scenario. These results are consistent with the analysis of first harmonics presented in Fig. 3.

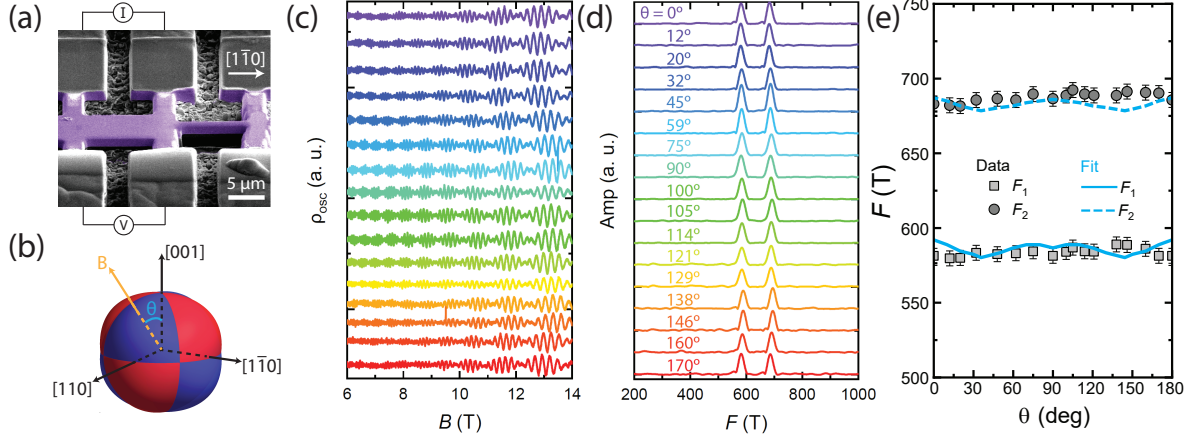


FIG. S13. (a) SEM image of device-2. Here the gold thin film is covered with FIB-deposition of Carbon thin film (grey) for protection of ion beam tail during microstructure fabrication. The current is applied along  $[1\bar{1}0]$  axis. (b) Demonstration of field and current orientation of SdH measurements. For device-2 the magnetic field is applied within the  $(1\bar{1}0)$  plane, and  $\theta$  is defined as the angle between the applied field and  $[001]$  axis. (c) Angular dependence of SdH oscillations  $\rho_{osc}$ . (d) FFT spectrum of SdH oscillations. Again two and only two mean frequencies are observed. (e) Angular dependence of SdH oscillation frequencies and theoretical prediction which successfully reproduced the experimental results.

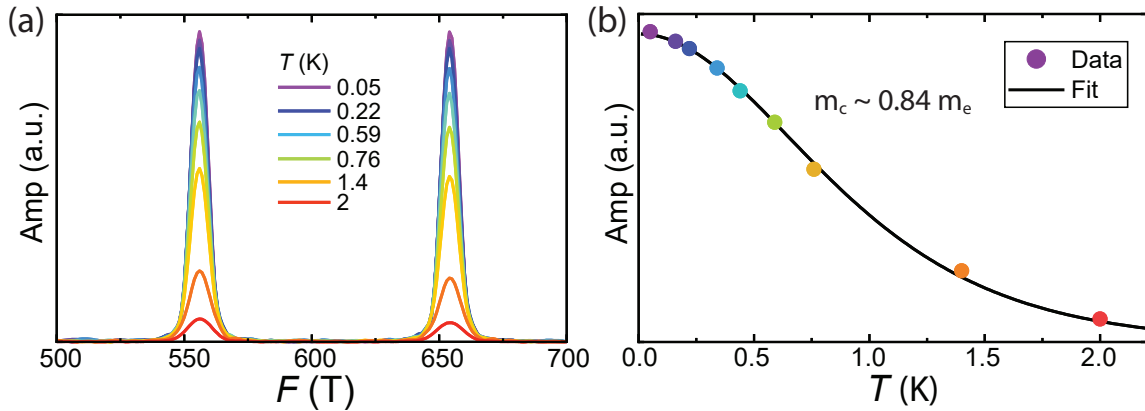


FIG. S14. (a) Fast-Fourier-Transformation spectrum of the SdH oscillations presented in Fig. 3(a) with the field window of 3 to 14 T. Two main peaks can be clearly observed. The suppression of peak amplitude with increasing temperature is due to the thermal damping effect. (b) Lifshitz-Kosevich fit to the temperature dependence of cyclotron mass. The fitting yields a cyclotron mass  $m_c \sim 0.84 m_e$ , comparable to the previously reported values<sup>7,8</sup>.

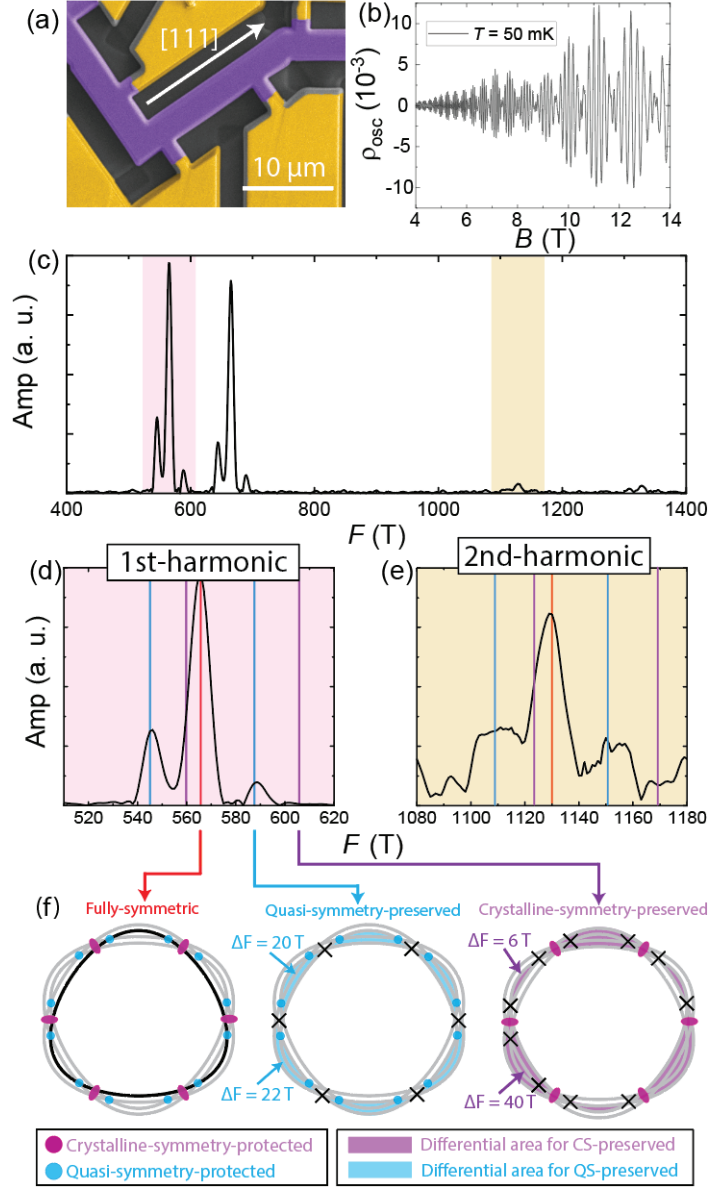


FIG. S15. (a) Scanning electron microscope image of CoSi microdevice with a short bar along [111] direction (device-4). This configuration generates a tensile strain along [111] which breaks all  $C_2$  rotation symmetries. (b) SdH oscillations with field and current applied along [111] axis at  $T = 50$  mK. (c) FFT spectrum of SdH oscillations. (d) Enlarged view of satellite peaks correspond to the 1<sup>st</sup> and 2<sup>nd</sup> harmonic oscillations. The red, purple and blue vertical lines correspond to the FFT spectrum produced by the fully symmetric, crystalline-symmetry-preserved and quasi-symmetry-preserved scenarios respectively. (e) Corresponding Landau orbits for three different scenarios. Here the colored area illustrates the orbital area difference compared to the fully-symmetric case. Only the quasi-symmetry-preserved scenario reproduces FFT peaks that match well with the experimental data.

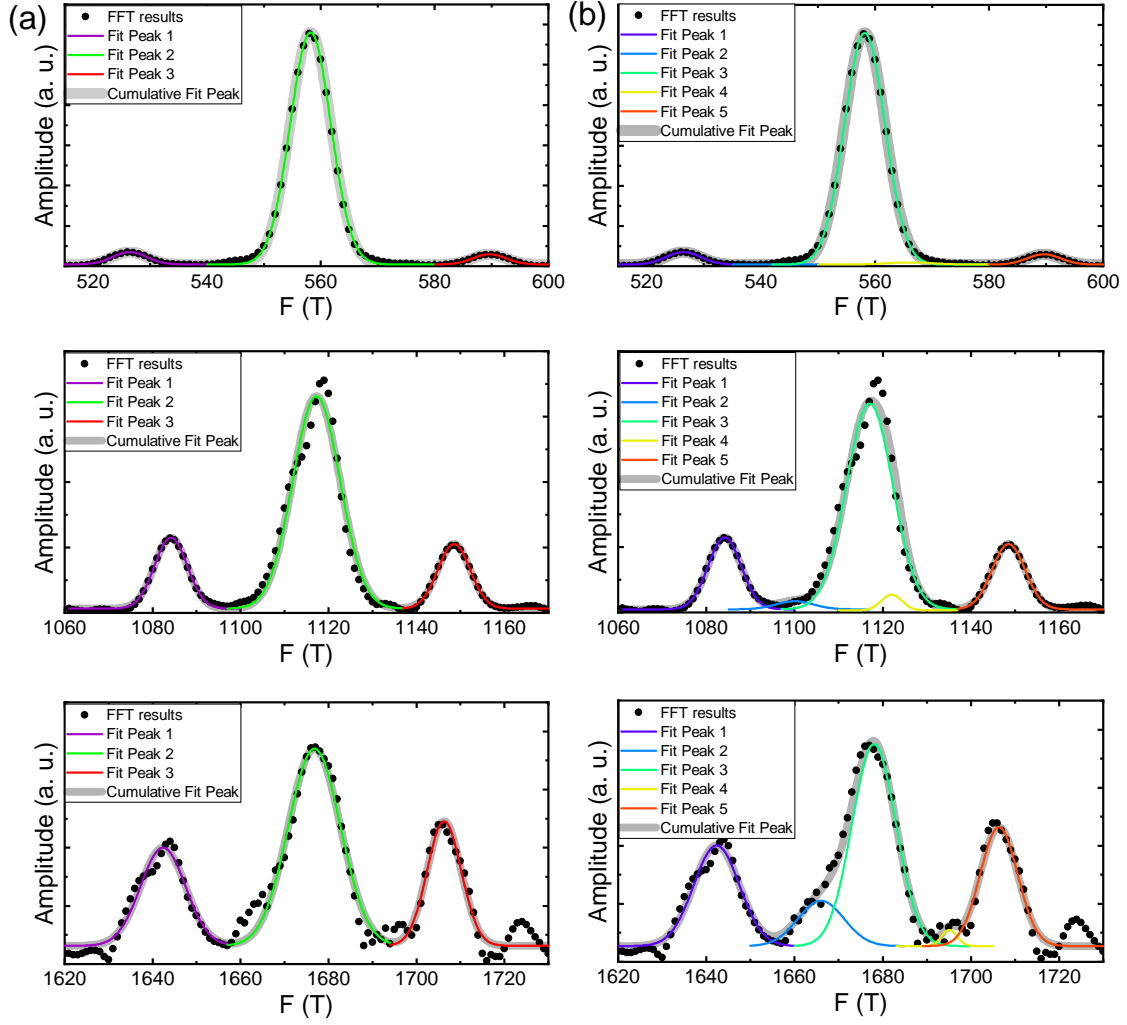


FIG. S16. 3-peak (a) and 5-peak (b) Gaussian fitting of the FFT spectrum of quantum oscillations measured with field and tensile strain applied along [110] axis at  $T = 50$  mK.

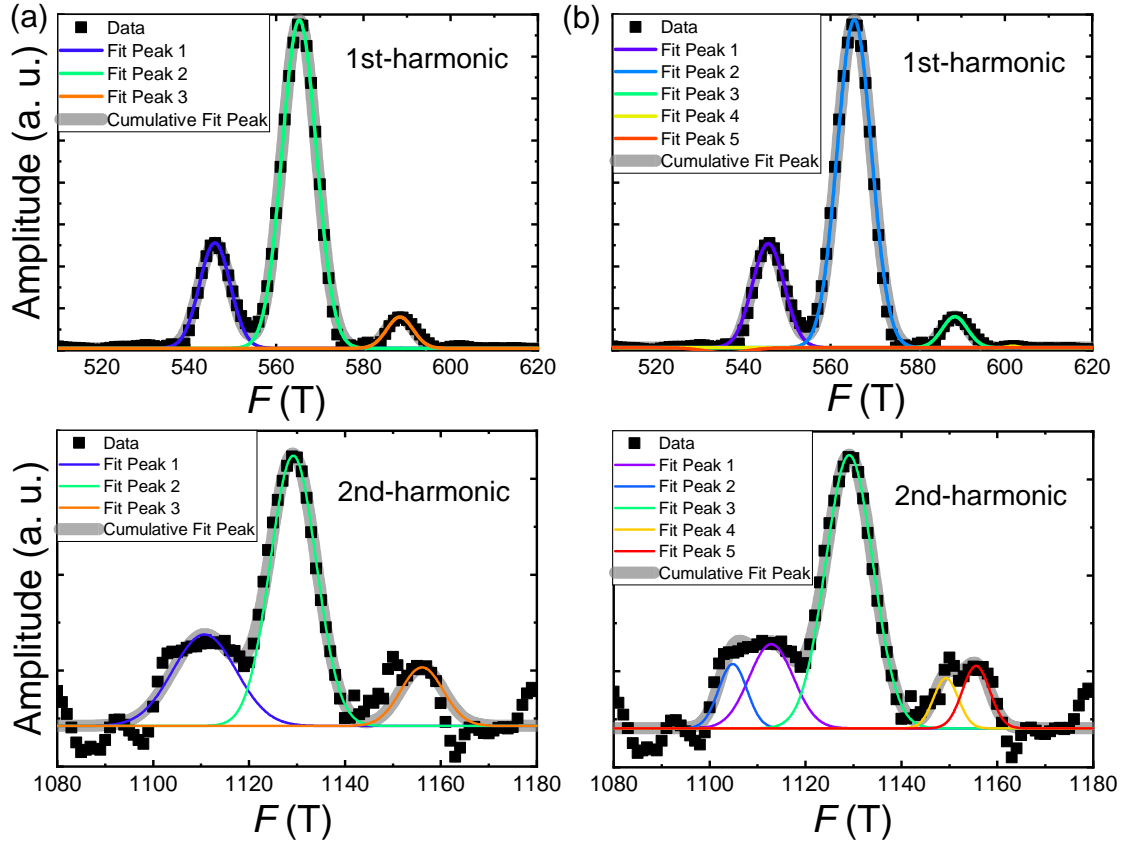


FIG. S17. 3-peak (a) and 5-peak (b) Gaussian fitting of the FFT spectrum of quantum oscillations measured with field and tensile strain applied along [111] axis at  $T = 50$  mK.

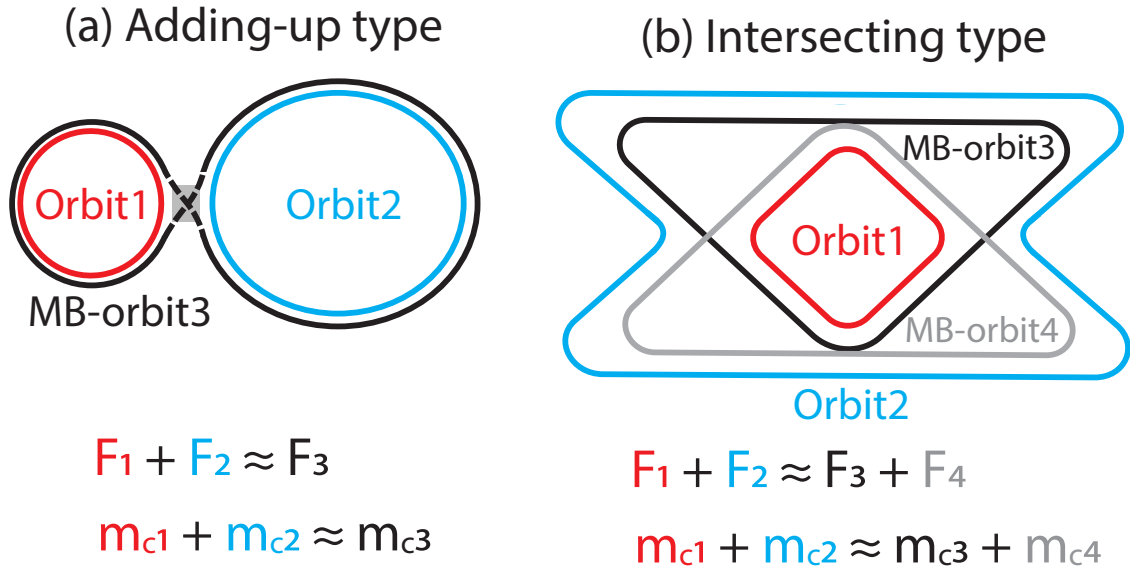


FIG. S18. Illustration of different magnetic breakdown scenarios. For the adding-up type, according to semi-classical theory, the oscillation frequency and cyclotron mass of the breakdown orbit can be simply calculated by summing up the values from the original orbits. While for the intersecting type since there exists more than one breakdown orbits the situation is more subtle.

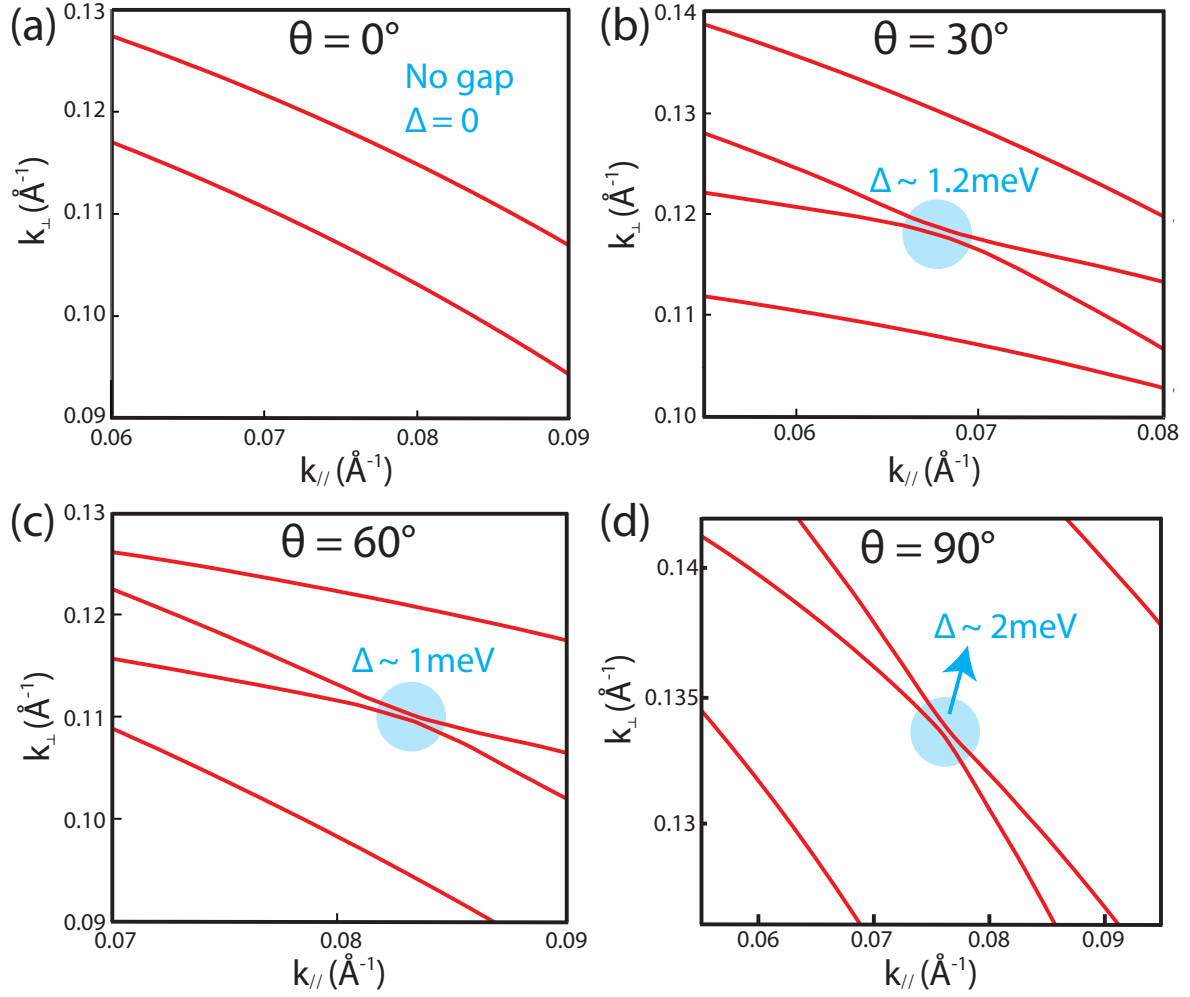


FIG. S19. Fermi surface orbits with field applied along different directions obtained from DFT band structure calculations. Here  $\theta$  is defined the same as in Fig. S3(a). The largest estimated breakdown gap  $\Delta \approx 2$  meV occurs when field is applied along  $[110]$  axis ( $\theta = 90^\circ$ ).



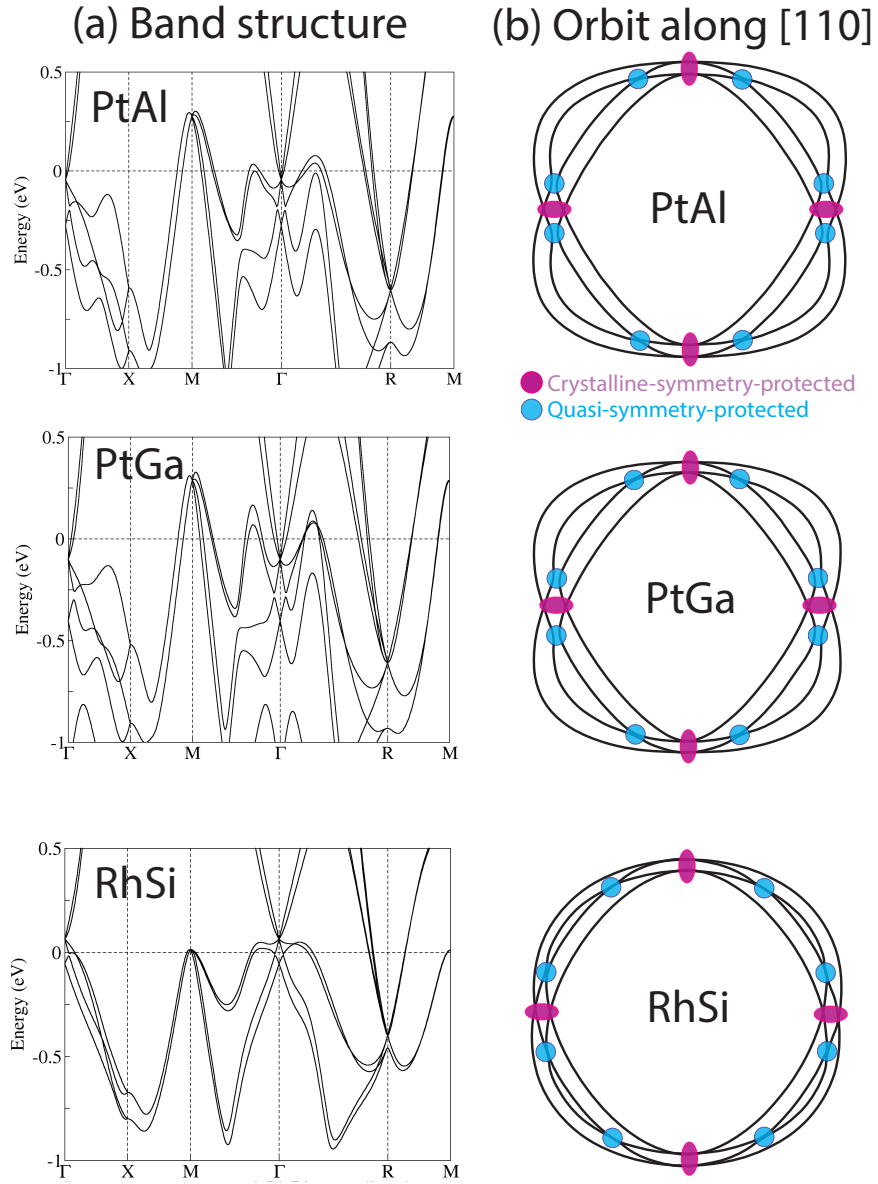


FIG. S20. (a) Band structure calculation of PtAl, PtGa and RhSi. The similarity of electronic structure among these materials are expected as they share the crystal structure. (b) Fermi surface orbits with field applied along [110] axis for all three materials. The crystalline symmetry and quasi-symmetry-protected degeneracies are denoted with purple and blue circles respectively.

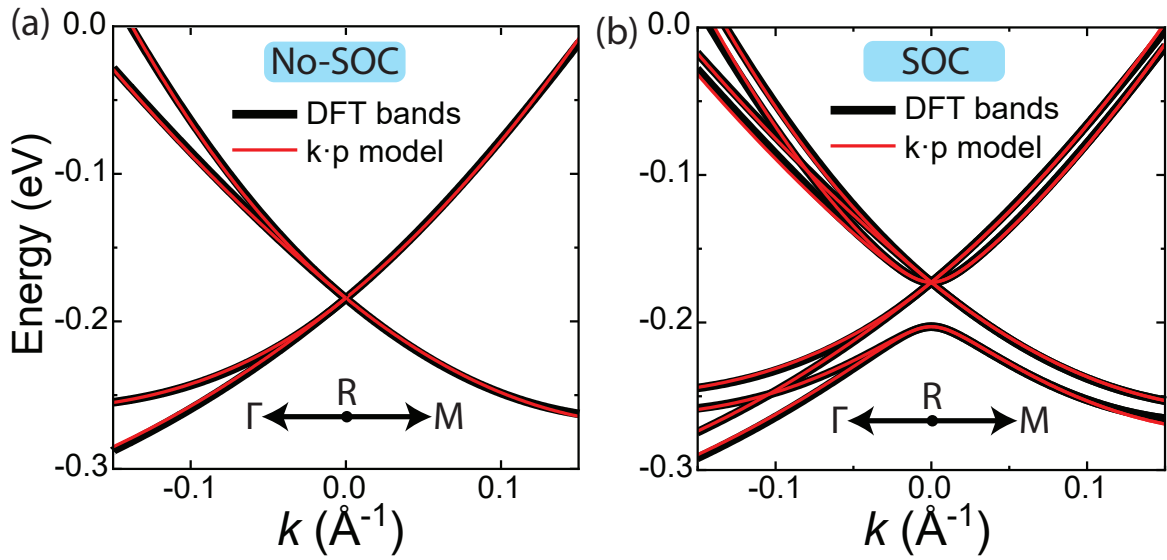


FIG. S21. DFT-calculated Band structures (black) and  $k \cdot p$  model fitting (red) around the  $R$ -point. (a) The fitting along the  $R - M$  line generates parameters  $C_0, A_1, B_1$  for the  $\mathbf{k} \cdot \mathbf{p}$  Hamiltonian without SOC. The remaining parameters  $C_1, C_2, C_3$  are obtained for the  $\mathbf{k} \cdot \mathbf{p}$  Hamiltonian without SOC along the  $R - \Gamma$  line. (b) Fitting the strength of SOC  $\lambda_0$  for the  $\mathbf{k} \cdot \mathbf{p}$  Hamiltonian with SOC (the  $R$ -model) along the  $\Gamma - R - M$  line.

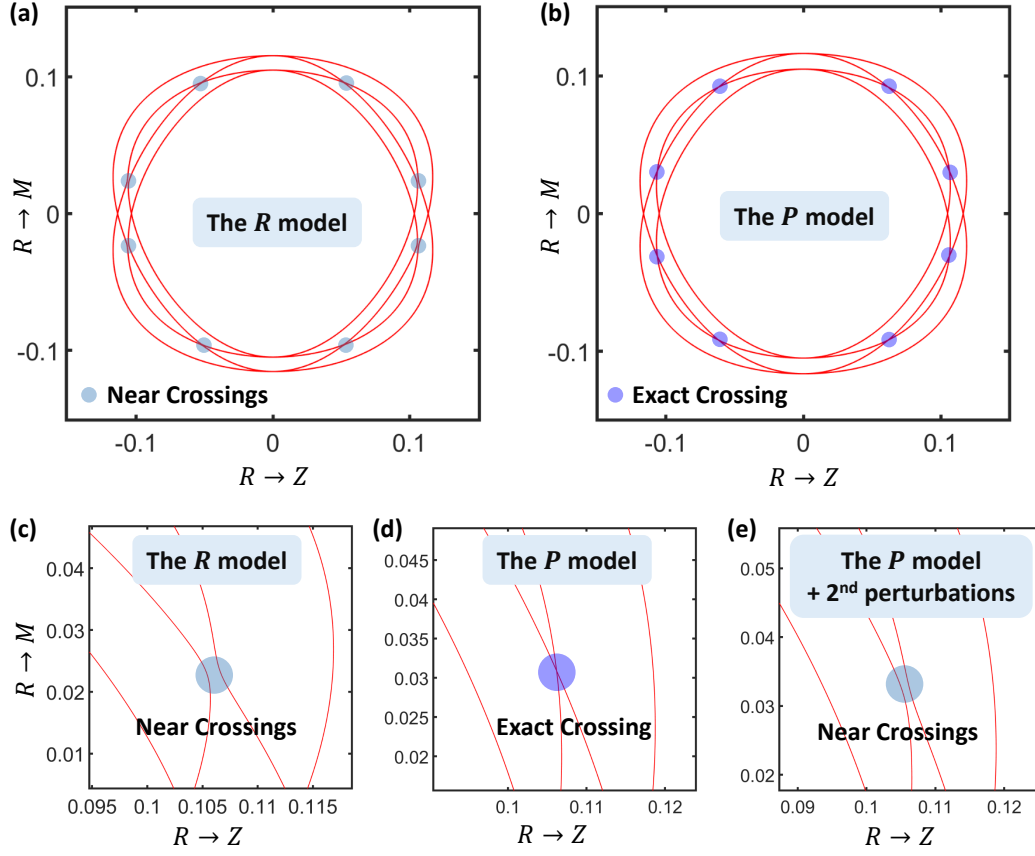


FIG. S22. Fermi surfaces at  $E_f = -0.06$  eV in the  $\Gamma - R - M$  plane. (a) Fermi surfaces generated from the  $R$ -model, eight near crossings are found and marked by light-blue solid circles. As a comparison, the Fermi surfaces for the  $P$ -model is shown in (b), which display eight exact crossings (marked by purple solid circles). The zoomed plots for the near/exact crossings are shown in (c),(d) and (e). (c)  $R$ -model calculations indicate a very tiny gap for the near crossings. (d) The exact crossings in  $P$ -model with only first order perturbation is shown for a comparison, of which the two-fold degeneracy is protected by the quasi-symmetry. (e) After adding the second-order perturbation corrections to the  $P$ -model, the quasi-symmetry is broken and thus the exact crossings are gapped. In all figures, the unit for energy is eV and that for momentum is  $\text{\AA}^{-1}$ .

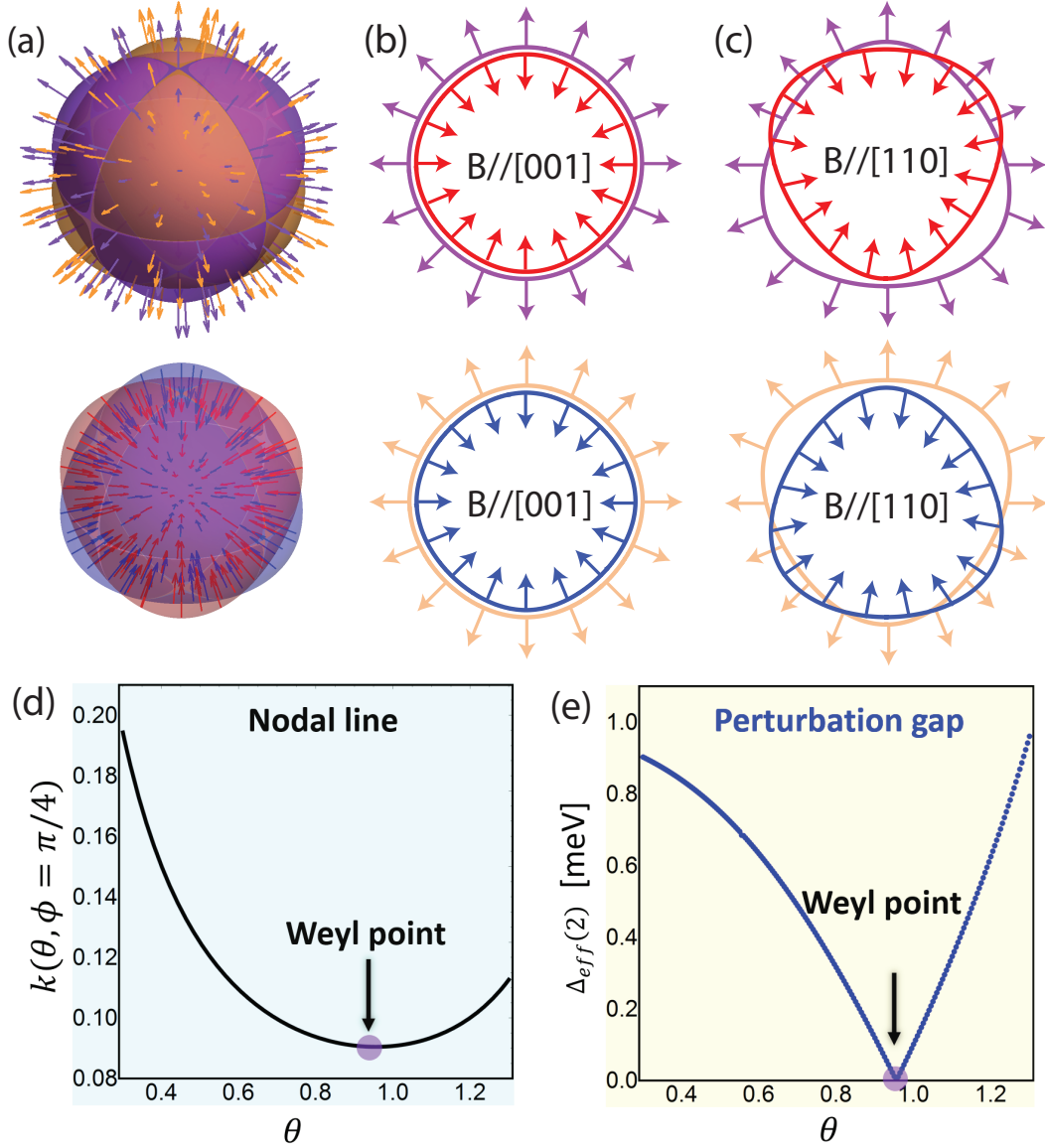


FIG. S23. (a) The spin texture (colored arrow) for all four Fermi surfaces calculated from the  $P$ -model. As discussed in the main manuscript, since the spin of the eigen-states is parallel or anti-parallel to the momentum, Fermi surfaces with different spin character(+/-) have opposite spin-polarization at the same momentum. (b) and (c) present the spin texture of Fermi surface orbits with field applied along [001] and [110] direction respectively. (d) Nodal line on the  $\Gamma - R - M$  plane with  $\theta \in \{0, \pi/2\}$  and  $\phi = \pi/4$  obtained by solving  $d_z(\mathbf{k}) = 0$  in Eq. (S49). (e) Energy gap on the nodal line caused by the second-order perturbation corrections,  $\delta_{eff(2)} = 2\sqrt{(\delta d_x)^2 + (\delta d_y)^2}$ , in unit of meV. This gap is resulted from the second-order perturbation which involves the spin-flipping terms. The momentum  $k$  is in unit of  $\text{\AA}^{-1}$ .

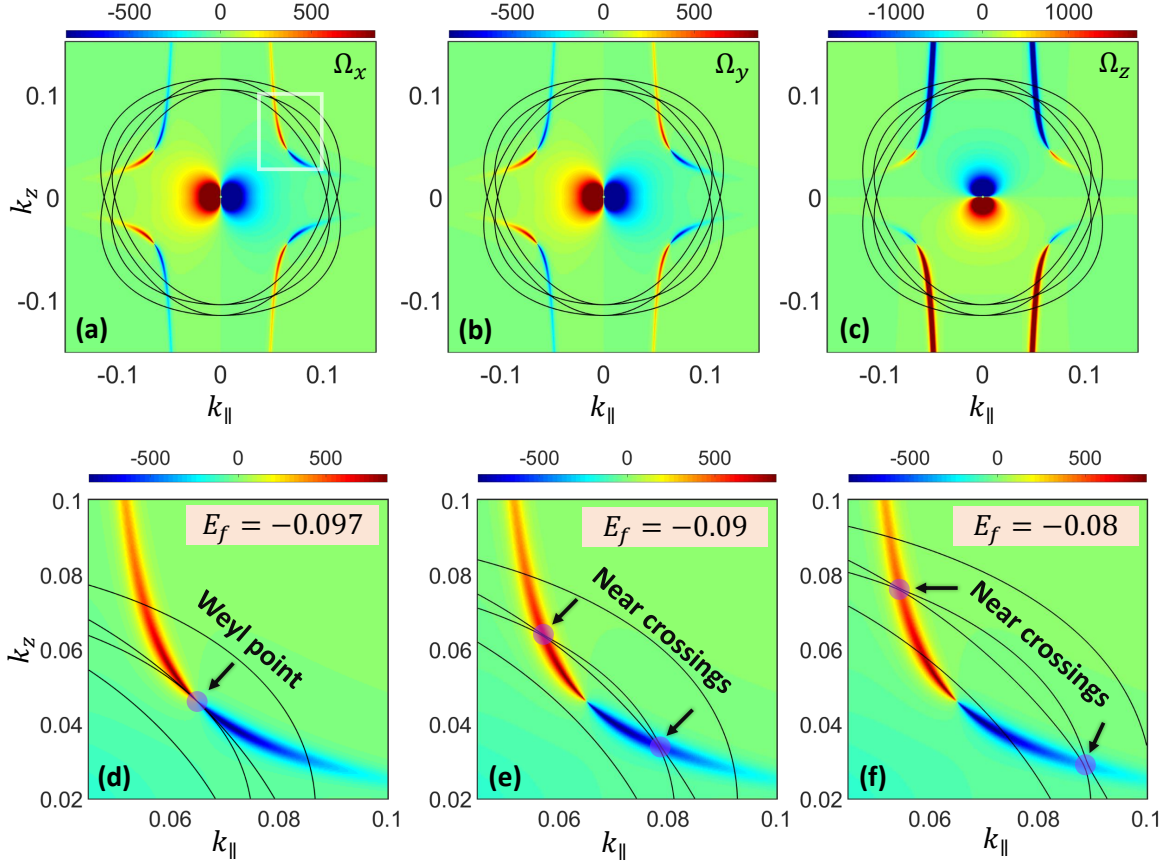


FIG. S24. The Berry curvature distributions around the near crossings on the  $\Gamma - R - M$  plane. In (a),(b) and (c), the three component of the Berry curvature ( $\Omega_{x,y,z}$ ) are shown for the the  $1^-$ -band. The black lines stand for the Fermi surface contour with  $E_f = -0.06$  eV. The zoomed plot for  $\Omega_x$  in (a) is shown in (d),(e) and (f), where we compare the Fermi surface flow as the distributions of  $\Omega_x$ . The Fermi energies are  $E_f = -0.097$  eV,  $E_f = -0.09$  eV,  $E_f = -0.08$  eV for (d), (e), and (f), respectively. The singularity is at the type-II Weyl points, as well as that for the 6-fold degeneracy at the  $R$ -point. And the large Berry curvature almost sits at the near crossings (marked by the dark-red solid circles) on the Fermi surface. In all figures, the unit for energy is eV and for momentum it is  $\text{\AA}^{-1}$ .

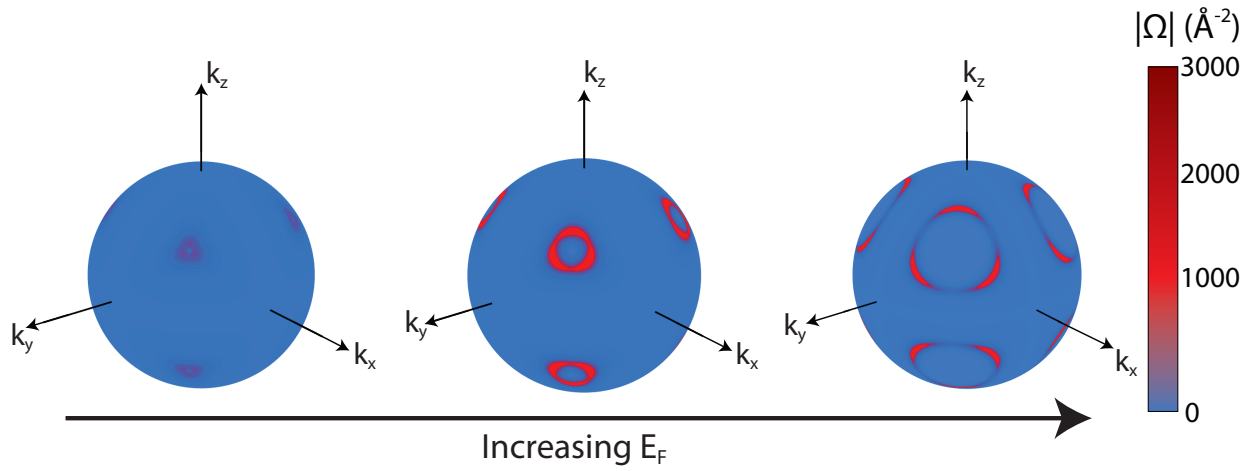


FIG. S25. Energy-dependent Berry curvature in momentum space for the  $1^-$ -band. The large Berry curvature is a direct result of near-degeneracy due to quasi-symmetry.

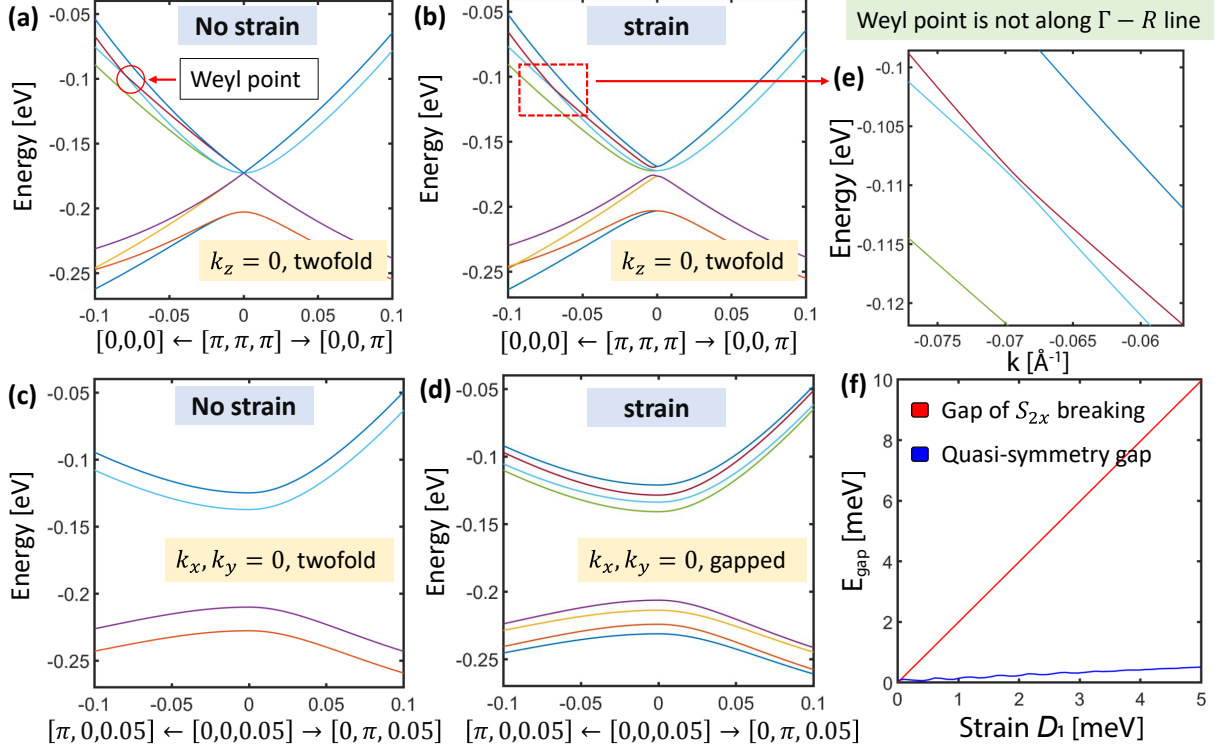


FIG. S26. The bands without/with strain effect. To model the [110] strain that breaks both  $S_{2x}$  and  $S_{2y}$  screw rotations, we use  $D_1 = 0.003$ ,  $D_2 = 0.001$ , and  $D_3 = 0.002$  in unit of eV. However, the  $S_{2z}$  rotation is preserved for the [110] strain. In (a) without strain and (b) with strain, we can see the bands along  $k_z = 0$  line are still degenerate. However, in (c) and (d), the bands along  $k_x, k_y = 0$  are no longer degenerate due to strain effect (crystalline symmetry breaking). In (e), the Weyl point is no longer along the  $\Gamma - R$  line since the  $C_3$  rotation is broken. In (f), the band gap due to the breaking of  $S_{2x}$  and the quasi-symmetry gap are shown for the bands in the  $\Gamma - R - M$  plane, which indicates that the quasi-symmetry is almost unaffected by the strain. In this schematic plot, we set  $D_2 = D_3 = 0$  and  $D_1 \neq 0$  for [110] strain. At zero strain ( $D_1 = 0$ ), the gap for the  $S_{2x}$  breaking is exactly zero; while the quasi-symmetry gap is small  $\sim 0.1$  meV.

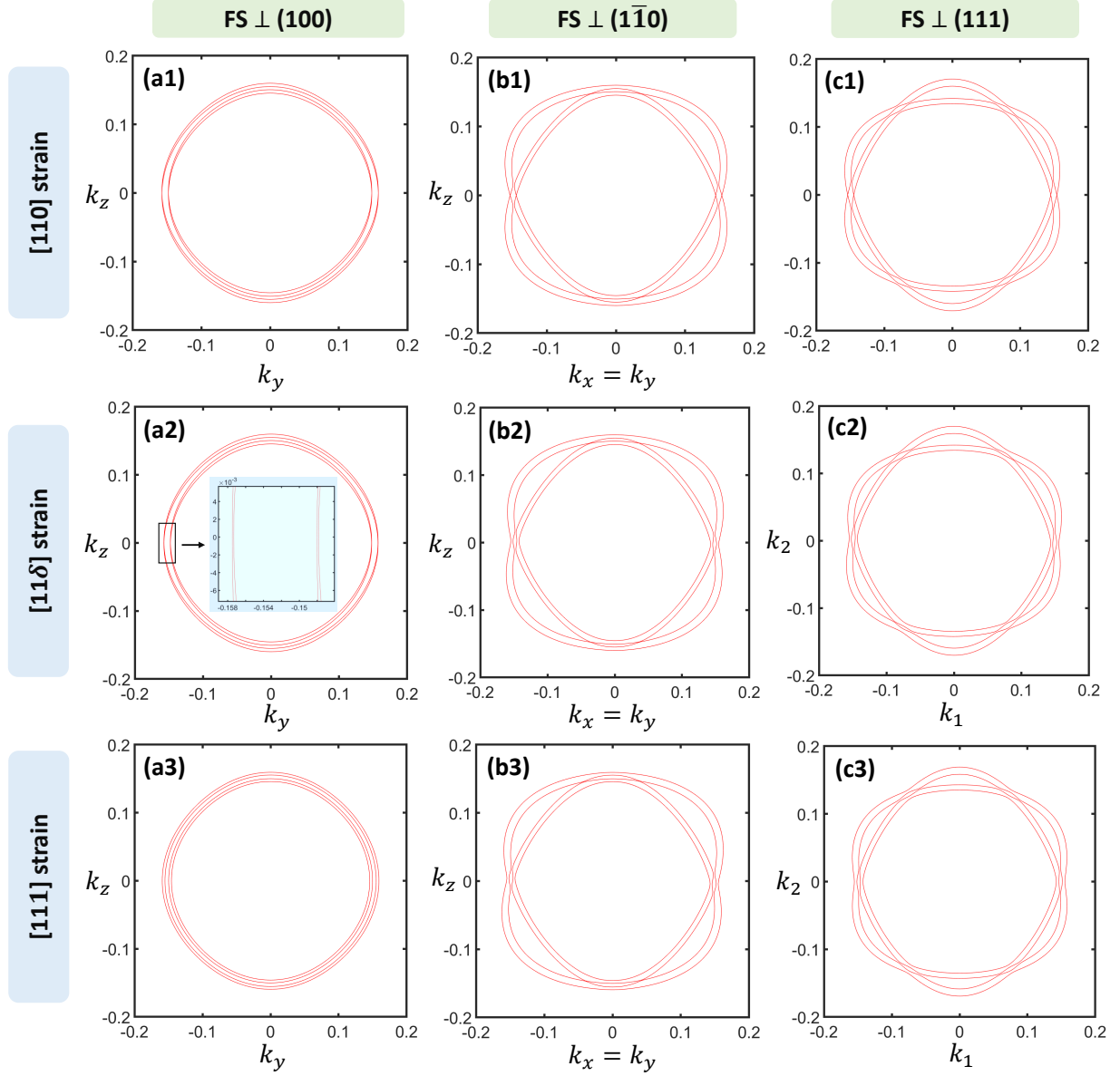


FIG. S27. The Fermi surfaces in planes perpendicular to the (100),  $(1\bar{1}0)$  and (111) axes for three types of strain effect: [110] strain (breaks  $S_{2x}$  and  $S_{2y}$ ), [11 $\delta$ ] strain (breaks all crystalline symmetries) and [111] strain (breaks  $S_{2x}$ ,  $S_{2y}$  and  $S_{2z}$ ), respectively. In (a1, b1, c1), the Fermi surfaces for the [110] strain ( $D_1 = 0.003$ ,  $D_2 = 0.001$ , and  $D_3 = 0.002$  in unit of eV). In (a2, b2, c2), the Fermi surfaces for the [11 $\delta$ ] strain ( $D_1 = 0.003$ ,  $D_2 = 0.001$ ,  $D_3 = 0.002$  and  $D_4 = 0.004$  in unit of eV). In (a3, b3, c3), the Fermi surface for the [111] strain ( $D_1 = 0.003$  in unit of eV). Note that a possible  $D_4$  as the same order as other parameters is assumed for the illustration of the Fermi surface plot where  $S_{2z}$  rotation is also broken so that the degeneracy at  $k_z = 0$  is broken.



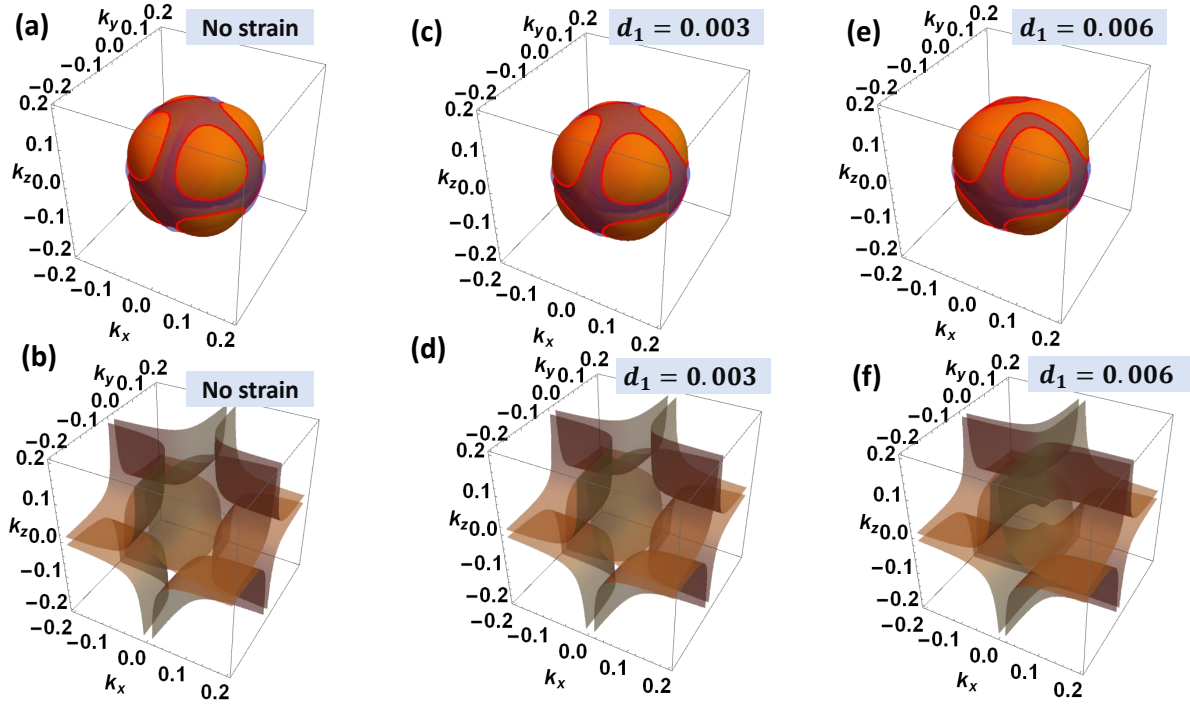


FIG. S28. The quasi-symmetry protected nodal planes with/without strain effect. In (a, c, e), the two Fermi surfaces of the P-model show the intersecting features (see the red lines). In (b, d, f), the quasi-symmetry protected nodal planes are found for both without and with strain effects.